ANALYSIS OF NANOSCALE INGREDIENTS IN COMMERCIAL FOOD AND COSMETIC PRODUCTS BY FIELD-FLOW FRACTIONATION AND SINGLE PARTICLE ICP-MS

By

Lyndon Naidoo

(Reg. No: 21353659)

Submitted in fulfilment of the requirements of the degree of Master of Applied Sciences in Chemistry in the Faculty of Applied Sciences at the Durban University of Technology

September 2020

DECLARATION

I, **Lyndon Naidoo,** declare that the thesis submitted for the degree of Master of Applied Sciences (MAppSci): Chemistry at the Durban University of Technology is the result of my own investigation and has not already been accepted in substance for any degree, and is not being concurrently submitted for any other degree. All the work was done by the author.

Student Name: Mr. L. Naidoo

Signature: Date

Supervisor Name: Prof Krishna Bisetty

Signature: Date:

Co-Supervisor Name: Dr Suvardhan Kanchi

Signature: Date:

Co-Supervisor Name: Dr Myalowenkosi I Sabela

Signature: Date:

ACKNOWLEDGEMENTS

It is by no means possible that I would have made it without the following set of inspirational people in my life. But before I make mention of them, I would like to thank God for guiding and helping me realise my dreams, placing me in a position to catapult towards success to infinity and beyond.

I would like to start by thanking my supervisors, Prof Krishna Bisetty, Dr Suvardhan Kanchi and Dr Myalowenkosi Sabela for shepherding me through the trials and tribulations of the plight of a novice researcher. Their continuous input and guidance have proven invaluable from day one.

I would also like to extend my gratitude to my CMBAC (Computational Modelling and Bio-Analytical Chemistry) research group members, namely Phathisanani Hloma, Senzekile Majola, Matshidiso Lephalala, Nomnotho Jiyane, Calvin Harilal and Kwanele Kunene, for the countless moments of support and encouragement. Special mentions go out to Mrs NM Xhakaza, Ms N P Cele and Mrs D Naicker for the unwavering assistance in the lab.

My gratitude also extends to the group of special international experts that visited throughout the project duration, namely Mr Tony Pfaffe, Dr Helmut Ernstberger, Mrs Evelin Moldenhauer and Mr Achim Schmottlach. My eternal gratitude for their exciting insights and influence on my work.

Acknowledgements go out to the National Research Foundation (NRF) of South Africa, Durban University of Technology and the Centre for High Performance Computing (an

initiative supported by the Department of Science and Technology in South Africa) for financial support and access to cutting-edge resources to make this work possible.

Finally, I would like to thank all my family and friends who have persisted to stick by my side throughout this gruelling yet exciting journey. You all have helped me stay on track and march on to the light at the end of the tunnel.

ABSTRACT

There is a growing need to disclose the possible presence of nanostructures on the labels of commercial food and cosmetic products in South Africa. Synthetic amorphous silica (SiO_2) and titanium dioxide (TiO_2) are the two widely used nanoparticles (NPs) selected for this study. This work was undertaken in two stages. The first part deals with an analytical method developed for the separation and characterization of TiO_2 NPs capped with poly(ethylene glycol) (PEG) as a potential reference material for sunscreen analysis. The second aspect of this work focuses on SiO_2, a highly attractive biomaterial widely used as a food additive (E551) to improve the flow properties of powdered food ingredients. Also, modern computational methods were implemented in both case studies, to better understand the nanoparticulate interactions with the organic substrates at an atomistic and molecular level.

For the cosmetics study, asymmetric flow field-flow fractionation (AF4) coupled online to multi-angle light scattering (MALS) and dynamic light scattering (DLS) detectors were employed to assess the geometry and size of the PEGylated TiO_2 NPs in terms of the evaluated radius of gyration (r_g) and hydrodynamic radius (r_h). Single particle inductively coupled plasma mass spectrometry (spICP-MS) and transmission electron microscopy (TEM) were implemented to provide information on the core diameter (d) of the TiO_2 particle. To overcome agglomeration, Monte Carlo simulations were employed in this study to assess the effectiveness of PEG capped onto spherically constructed TiO_2 anatase nanoclusters by systematically performing a series of adsorption studies. For PEG-TiO_2 NPs, AF4-MALS-DLS reported r_g and r_h values of 28.7 nm and 40.3 nm respectively, with the shape factor (r_g/r_h) values generally reported in the range of 0.7 to 0.8, indicative of spherical particle geometry. SpICP-MS and TEM obtained complementary measurements of d = 32.0 nm and d = 38.4 nm, respectively. The computational modelling results demonstrated the strong binding affinity of

PEG as a capping agent to TiO_2, exhibiting stabilisation of TiO_2 NPs in aqueous medium. Finally, the developed AF4-MALS-DLS method was applied to two commercial SPF 50 sunscreens, exhibiting promising separation and detection efficiency. These findings can contribute to regulatory measures in line with the South African National Nanotechnology Strategy for the cosmetics industry.

With regards to the food application study, a multivariate method was developed for the detection and characterization of SiO_2 particles also based on AF4-MALS-DLS. This analytical approach attempts to address the fate and the presence of nanoparticulate SiO_2 additives (E551) in food products. The experimental design using SiO_2 NP standards resulted in the following optimum conditions of the system: crossflow, 0.8 ml/min; injection time, 5 min and sonication time, 60 min. It was observed that the average geometric diameters (D_{geo}) for SiO_2 NPs in three selected commercial coffee creamers (A, B and C) detected by AF4-MALS were 286.7 nm, 129.8 nm and 190.7 nm respectively. Similar trends for the coffee creamers were observed for the hydrodynamic diameter (D_h) measurements using AF4-DLS i.e. 301.5 nm, 141.3 nm and 197.8 nm respectively. The r_g/r_h values were reported ranging from 0.7 to 0.8, indicative of spherical particle geometry. Also, the electrostatic interactions between SiO_2 NPs and glucose/water mixtures, as evaluated by Monte Carlo simulations, revealed O-interactions dominating over the flat amorphous SiO_2 surface. The strongest interaction observed (around -239 kcal/mol) for the SiO_2-water/glucose mixture demonstrates the hydrophilic nature of SiO_2 NPs.

The findings in both case studies provide fundamental information to improve the understanding of nanoparticulate interactions with additives and paves the way for the labelling of cosmetic and food products that potentially exhibit nanomaterials in complex matrices.

LIST OF CONFERENCE PRESENTATIONS AND PUBLICATIONS

Publications

Lyndon Naidoo, Suvardhan Kanchi, Myalowenkosi I. Sabela, and Krishna Bisetty. **2020**. Multivariate optimization of field-flow fractionation of nanoscale synthetic amorphous silica in processed foods supported by computational modelling. *New Journal of Chemistry*, 44 (40): 17542-17551.

Lyndon Naidoo, Suvardhan Kanchi, Myalowenkosi I. Sabela, and Krishna Bisetty. **2020**. Investigation of TiO_2 nanoscale ingredients in sunscreens by AF4-MALS-DLS and spICP-MS supported by computational modelling. *Microchemical Journal* (Ref: MICROC_2020_1963, Under Revision).

Oral Presentations

Lyndon Naidoo. "Analysis of TiO_2 nanoscale ingredients in cosmetic products by Field-Flow Fractionation". **4th** Interdisciplinary Research and Innovation Conference held at Hilton Hotel, Durban, South Africa. 17th to 20th September **2019**.

TABLE OF CONTENTS

DECLARATION ..... **I**

ACKNOWLEDGEMENTS ..... **II**

ABSTRACT ..... **IV**

LIST OF CONFERENCE PRESENTATIONS AND PUBLICATIONS ..... **VI**

TABLE OF CONTENTS ..... **VII**

LIST OF FIGURES ..... **XII**

LIST OF TABLES ..... **XV**

LIST OF ACRONYMS AND SYMBOLS ..... **XVI**

CHAPTER 1 - INTRODUCTION **1**

1.1) Analysis of nanoscale ingredients in food and cosmetics: Silicon Dioxide and Titanium Dioxide 1

1.2) Aims and objectives 2

1.3) Thesis outline 3

CHAPTER 2 - LITERATURE REVIEW **5**

2.1) TiO_2 nanoscale ingredients in cosmetics 5

2.2) Nanoscale synthetic amorphous silica in processed foods 8

CHAPTER 3 - THEORETICAL PRINCIPLES **12**

3.1) Experimental principles 12

3.1.1) Asymmetric Flow Field-Flow Fractionation (AF4) 12

3.1.2) Multi-Angle Light Scattering (MALS) 15

3.1.3) Dynamic Light Scattering (DLS) 20

3.1.4) Single Particle Inductively Coupled Plasma-Mass Spectrometry (spICP-MS) .. 22

3.2) Computational modelling 24

3.2.1) Monte Carlo (MC) simulation 24

CHAPTER 4 28

4.1) Experimental 28

4.1.1) Chemicals and reagents 28

4.1.2) Capping of TiO_2 NPs with PEG 29

4.1.3) Sample preparation of commercial sunscreens 29

4.1.3.1) spICP-MS 29

4.1.3.2) AF4-MALS-DLS 30

4.1.4) Instrumentation 30

4.1.4.1) AF4-MALS 30

4.1.4.2) AF4-DLS and zeta potential analysis 31

4.1.4.3) spICP-MS 31

4.1.4.4) TEM 31

4.1.5) Spectroscopic and thermogravimetric studies 32

4.1.6) Computational modelling methodology 32

4.1.6.1) Titanium dioxide nanoclusters 32

4.1.6.2) Poly(ethylene glycol) (PEG) 33

4.1.6.3) Adsorption studies of PEG and water onto TiO_2 nanoclusters 34

4.2) Results and discussion 34

4.2.1) Experimental 34

4.2.1.1) Optimization of AF4-MALS-DLS method 34

4.2.1.2) Size characterisation and distribution of PEG-TiO_2 NPs by AF4-MALS-DLS 37

4.2.1.3) Size characterisation and distribution of TiO_2 NPs in commercial sunscreens by AF4-MALS-DLS 38

4.2.1.4) Size characterisation and distribution of TiO_2 NPs by spICP-MS 41

4.2.1.5) Size characterisation of TiO_2 NPs by TEM 42

4.2.1.6) Zeta potential, spectroscopic and thermogravimetric characterisation of TiO_2 NPs and PEG-TiO_2 NPs 44

4.2.1.7) Summative particle size evaluation 46

4.2.2) Computational 48

4.3) Summary 49

CHAPTER 5 51

5.1) Experimental 51

5.1.1) Chemicals and reagents 51

5.1.2) Sample preparation of commercial coffee creamers for AF4-MALS-DLS 52

5.1.3) Instrumentation 52

5.1.3.1) AF4-MALS 52

5.1.3.2) AF4-DLS 53

5.1.4) Spectroscopic studies 53

5.1.5) Experimental design 53

5.1.6) Data analysis 54

5.1.7) Computational modelling methodology 54

5.1.7.1) Construction of nanostructures and Forcite-geometry-based structural analysis 55

5.1.7.2) Monte Carlo adsorption studies 55

5.2) Results and discussion 56

5.2.1) Experimental 56

5.2.1.1) BBD: Analysis of variance on analyte response 56

5.2.1.2) BBD: Interaction studies 59

5.2.1.3) Optimisation of AF4-MALS-DLS method 62

5.2.1.4) Size characterisation and distribution of SiO_2 NPs in commercial coffee creamers by AF4-MALS-DLS 63

5.2.1.5) Spectroscopic characterization of amorphous SiO_2 NPs 65

5.2.2) Computational 66

5.3) Summary 69

CHAPTER 6 – CONCLUSIONS AND FUTURE PERSPECTIVES 71

6.1) Conclusions 71

6.2) Future perspectives 72

REFERENCES **73**

APPENDICES **82**

LIST OF FIGURES

Figure 2.1. TiO_2 polymorphs used in sunscreen **(a)** anatase **(b)** rutile. The Ti and O atoms are denoted in grey and red, respectively. (The 3D structures for this study were generated using MS). 5

Figure 2.2. Layered structure of amorphous silica (SiO_2). The Si and O atoms are denoted in yellow and red respectively. (The 3D structures for this study were generated using MS). 9

Figure 3.1. Schematics of AF4 channel, reproduced with permission from Postnova Analytics GmbH, Germany (Postnova 2016). 13

Figure 3.2. Working principle of AF4 separation, reproduced with permission from Postnova Analytics GmbH, Germany (Postnova 2017). 14

Figure 3.3. Schematics of MALS detector, reproduced with permission from Postnova Analytics GmbH, Germany (Postnova 2017). 16

Figure 3.4. Light scattering principle of MALS detector, reproduced with permission from Postnova Analytics GmbH, Germany (Postnova 2017). 17

Figure 3.5. Schematics of DLS detector, reproduced with permission from Malm and Corbett (2019). 21

Figure 3.6. Aerosol desolvation, atomization and ionization in plasma, reproduced with permission from Montaño et al. (2016). 23

Figure 4.1. TiO_2 anatase simulated nanoparticles of sizes **(a)** 2 nm **(b)** 4 nm and **(c)** 6 nm. The Ti and O atoms are depicted in grey and red respectively. (The 3D structures for this study were generated using MS). 33

Figure 4.2. Simulated poly(ethylene glycol) chain. The C, H and O atoms are denoted in grey, white and red, respectively. (The 3D structures for this study were generated using MS). 33

Figure 4.3. AF4-MALS fractogram of uncapped TiO_2 NP suspension. 35

Figure 4.4. AF4-MALS fractogram overlays of 0.2 mg/ml PEG-TiO_2 NP suspension at different **(a)** crossflow rates and **(b)** injection volumes. In these fractograms, the supporting variables (injection volume in **(a)**; crossflow in **(b)**) have simultaneously been adapted to accommodate the varying variables (crossflow in **(a)**; injection volume in **(b)**) in view of possible inter-parameter interactions. 36

Figure 4.5. AF4-MALS-DLS fractograms of **(a)** r_g and r_h and **(b)** r_g/r_h over MALS 90° for 0.2 mg/ml PEG-TiO_2 NP suspension. 38

Figure 4.6. AF4-MALS-DLS fractograms of **(a)** r_g and r_h **(b)** r_g/r_h over MALS 90° for Nano-TiO_2 SPF 50 sunscreen. 39

Figure 4.7. AF4-MALS-DLS fractograms of **(a)** r_g and r_h **(b)** r_g/r_h over MALS 90° for Unspecified SPF 50 sunscreen. 41

Figure 4.8. SpICP-MS particle size distributions for **(a)** Uncapped TiO_2 NPs **(b)** PEG-TiO_2 NPs **(c)** Nano-TiO_2 SPF 50 and **(d)** Unspecified SPF 50 sunscreen samples. 42

Figure 4.9. TEM images for **(a)** Uncapped TiO_2 NPs **(b)** Nano-TiO_2 and **(c)** Unspecified SPF 50 sunscreen samples. 44

Figure 4.10. (a) UV spectrum **(b)** ATR-IR spectrum **(c)** TGA thermogram and **(d)** DSC thermogram of PEG, TiO_2 NPs and PEG-TiO_2 NPs. 45

Figure 4.11. Optimized structures showing adsorption of 50 PEG: 50 water units to TiO_2 particles of sizes **(a)** 2 nm **(b)** 4 nm and **(c)** 6 nm. (The 3D structures for this study were generated using MS). 49

Figure 5.1. Standardized Pareto chart for D_{geo} (MALS) response. 57

Figure 5.2. Interaction plot for D_{geo} (MALS) response. 60

Figure 5.3. Estimated response surface plot for D_{geo} (MALS) response of injection time vs sonication time at constant crossflow of 0.8 ml/min. 61

Figure 5.4. Contours of estimated response surface plot for D_{geo} (MALS) response of crossflow vs injection time at constant sonication time of 60 min. 61

Figure 5.5. AF4-MALS fractogram overlay of amorphous SiO_2 NP fractograms from Box-Behnken experimental design at MALS 90°. 62

Figure 5.6. AF4-MALS-DLS fractogram of amorphous SiO_2 NPs; crossflow = 0.8 ml/min, injection time = 5 min and sonication time = 60 min (**Run 2**). 63

Figure 5.7. AF4-MALS-DLS fractograms of **(a)** Sample A and **(b)** Sample B and **(c)** Sample C coffee creamer samples. 64

Figure 5.8. (a) UV spectrum **(b)** ATR-IR spectrum of amorphous SiO_2 NPs. 65

Figure 5.9. System conformations and distribution fields of ratios of SiO_2, water and glucose. The Si and O atoms are denoted in yellow and red respectively for SiO_2. With regards to water and glucose, the C, H and O atoms are depicted in grey, white and red, respectively. (The 3D structures for this study were generated using MS). 67

Figure 5.10. Overall total energy of SiO_2-water/glucose system. 68

LIST OF TABLES

Table 4.1. Summary of particle sizes evaluated from AF4-MALS, AF4-DLS, spICP-MS and TEM techniques (n = 3; associated ± error = STD Dev). 48

Table 4.2. Adsorption energy interactions of adsorbates to TiO_2 NPs. 49

Table 5.1. Box-Behnken experimental design of 15 runs and 3 parameters for AF4-MALS amorphous SiO_2 NP response. The discrete values are listed in **Appendix 3**..... 54

Table 5.2. ANOVA - Estimated effects based on total error and interactions. 58

Table 5.3. Correlation matrix showing extent of confounding interactions amongst effects. . 59

Table 5.4. Summary of particle sizes from AF4-MALS and AF4-DLS techniques (n = 3; associated ± error = Standard Deviation). 65

Table 5.5. Energy distribution (kcal/mol) of 10 adsorbates (water/glucose) onto the SiO_2 (substrate) surface. 68

LIST OF ACRONYMS AND SYMBOLS

AF4	Asymmetric Flow Field-Flow Fractionation
AL	Adsorption locator
ANOVA	Analysis of variance
ATR-IR	Attenuated Total Reflectance Infrared Spectroscopy
AuNP	Gold nanoparticle
BBD	Box-Behnken design
CCD	Central composite design
COMPASS	Condensed-phase Optimized Molecular Potentials for Atomistic Simulation Studies
D_{geo}	Geometric diameter
D_H	Hydrodynamic diameter
DLS	Dynamic Light Scattering
DW	Durbin-Watson
E551	Anti-caking agent
E_{ads}	Adsorption energy
EC	European Commission
E_{def}	Deformation energy
ENM	Engineered nanomaterial
EPA	Environmental Protection Agency
E_{rig}	Rigid adsorption energy
E_{tot}	Total energy
MALS	Multi-Angle Light Scattering

MC	Monte Carlo
MS	Material Studio
NM	Nanomaterial
NP	Nanoparticle
PEG	Poly(ethylene glycol)
PSD	Particle size distribution
QEq	Charge equilibrium
R_g	Radius of gyration
R_h	Hydrodynamic radius
R_g/R_h	Shape factor
ROI	Region of interest
RSM	Response surface methodology
SiO_2	Silicon dioxide
SPF	Sun Protection Factor
SpICP-MS	Single particle Inductively Coupled Plasma-Mass Spectrometry
TEM	Transmission Electron Microscopy
TGA/DSC	Thermogravimetric Analysis/Differential Scanning Calorimetry
TiO_2	Titanium dioxide
UV-Vis	Ultraviolet-Visible
V_c	Crossflow

CHAPTER 1 - INTRODUCTION

This chapter gives an overview of the underlying impact that engineered nanomaterials (ENMs) have on the global production of mainstream food and cosmetics concerning human health. The current technology available to potentially address the analytical problems on nanomaterial size regulations in products from the above-mentioned sectors is discussed. This is followed by the aims, objectives, and a brief outline of the thesis.

1.1) Analysis of nanoscale ingredients in food and cosmetics: Silicon Dioxide and Titanium Dioxide

Background and Problem Statement

Silicon dioxide (SiO_2) has been mainstream in the application of foodstuffs as an anti-caking agent for many years (Dekkers *et al.* 2011), while titanium dioxide (TiO_2) protects against UV radiation in sunscreens (López-Heras, Madrid and Cámara 2014). Studies have revealed both ingredients to contain nanoparticles (Barahona *et al.* 2015; Helsper *et al.* 2016; Zulfah and Siripinyanond 2018), which raises possible concerns on human consumption and usage.

As such, a huge impetus has been placed upon the quality control and toxicological evaluation of cosmetic and food products. International bodies such as the European Commission (EC) and the Environmental Protection Agency (EPA) have stressed the significance of nanomaterial regulation following the boom in production of engineered nanomaterials (ENMs) in the current industrial climate (Bocca *et al.* 2018). Upon consideration of these factors, several analytical methods have been evaluated for the size characterisation and quantification of SiO_2 NPs and TiO_2 NPs.

One of the most frequently used sizing techniques is dynamic light scattering (DLS). Its quick run times offer high analysis throughput potential, however, unwanted nanoparticle interaction interference within complex sample matrices remain an ongoing method sensitivity challenge (Malm and Corbett 2019).

Single particle inductively coupled plasma-mass spectrometry (spICP-MS) is known to obtain sensitive and mixed results for TiO_2 NPs and SiO_2 NPs respectively, but the technique itself is seen to be constrained by the need for high-level expertise and complicated procedures (Bolea-Fernandez *et al.* 2017; Zhao *et al.* 2018a). Asymmetric flow field-flow fractionation coupled to ICP-MS (AF4-ICP-MS) is a hyphenated technique in which the AF4 component is used to separate particles to subsequently be detected by ICP-MS for element identification and quantification, albeit with varying degrees of success (Nischwitz and Goenaga-Infante 2012; Heroult *et al.* 2014; López-Heras, Madrid and Cámara 2014; Aureli *et al.* 2015; Barahona *et al.* 2016; Helsper *et al.* 2016).

However, it has been noted that AF4 coupled to the multi-angle light scattering detector (AF4-MALS) is a promising technique employed in the physicochemical evaluation of nanoparticles in complex matrices, with further online coupling to DLS (AF4-MALS-DLS) the focus in this work.

1.2) Aims and objectives

Aim

The study is aimed at developing selective methods for the size characterization and quantification of silica and titanium dioxide nanoparticles by AF4-MALS-DLS and spICP-MS supported by computational modelling in food and cosmetic products, respectively.

Objectives

The objectives of this thesis are to:

- Perform characterization studies on commercially available TiO_2 NPs and SiO_2 NPs
- Develop methods for the separation and quantification of these nanoparticles by AF4-MALS-DLS

- Evaluate the analytical performance of the developed methods using real commercial samples
- Perform computational studies as a complementary tool to assess the aforementioned NPs behaviour in their respective interaction systems

1.3) Thesis outline

This thesis is divided into six chapters. Following the introduction, further chapters are divided as follows:

Chapter 2 - Literature Review

The chapter describes the literature survey of the project in terms of Case Studies I and II, with regards to the global production of ENMs amidst potential toxicological concerns on TiO_2 NPs and SiO_2 NPs, respectively. Also, the technology available along with analytical approaches to deal with each case study are discussed.

Chapter 3 - Theoretical Principles

This chapter deals with the theoretical principles underlying the experimental study, namely of the AF4, MALS, DLS and spICP-MS instrumentation. Aspects pertaining to the computational study viz. Monte Carlo simulation principles are also discussed.

Chapter 4 - Case Study I – Investigation of TiO_2 nanoscale ingredients in sunscreens by AF4-MALS-DLS and spICP-MS supported by computational modelling

This chapter details the method development of the size characterization and quantification of TiO_2 NPs in sunscreens by AF4-MALS-DLS and spICP-MS. It depicts the methodology and results of both experimental and supporting computational work.

Chapter 5 - Case Study II – Multivariate optimization of Field-Flow Fractionation of nanoscale synthetic amorphous silica in processed foods supported by computational modelling

A factorial experimental design was established and implemented to optimize the method development of the analysis of SiO_2 NPs in coffee creamer by AF4-MALS-DLS. All experimental trials, results and discussions along with supporting computational findings are included in this chapter.

Chapter 6 – Conclusions and future perspectives

A summary of the overall conclusions with possible future work is presented in this chapter.

References

A list of references cited throughout the thesis.

CHAPTER 2 - LITERATURE REVIEW

This chapter presents the case studies concerning the presence of TiO_2 and SiO_2 nanoparticles in cosmetics and processed foods, respectively. In short, discussions on the ubiquity of these nanomaterials in the current industrial climate are highlighted. Also, the potential human health concerns of their uses are elaborated on. Finally, techniques and analytical approaches suited for nanomaterial separation and size characterization in complex matrices are discussed.

2.1) TiO_2 nanoscale ingredients in cosmetics

Titanium dioxide (TiO_2) is one of the most widely employed nanomaterials in personal-care products and cosmetics. Often used in sunscreens, it may constitute up to 10% of the product by mass (Zhao *et al.* 2018a). Two crystal structures of TiO_2 nanoparticles (TiO_2 NPs) used in cosmetics are rutile and anatase (**Figure 2.1**), with the latter being more chemically reactive (Shi *et al.* 2013). Hence, rutile should be the preferred option for sunscreen synthesis however, studies report the use of anatase in products, or a mixture of both (Bunhu, Kindness and Martincigh 2011).

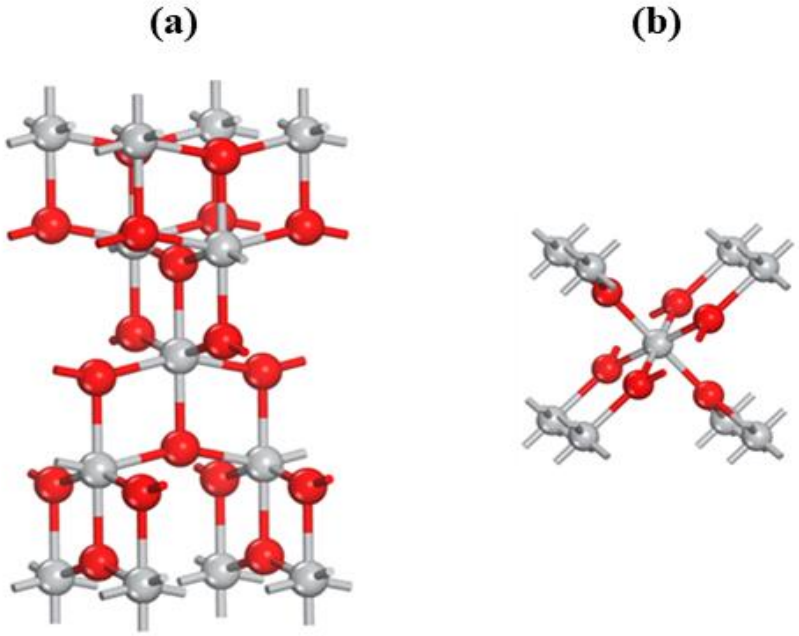

Figure 2.1. TiO_2 polymorphs used in sunscreen **(a)** anatase **(b)** rutile. The Ti and O atoms are denoted in grey and red, respectively. (The 3D structures for this study were generated using MS).

Figure 2.1 presents the geometric structures of anatase and rutile in respective unit cells. The anatase polymorph constitutes of repetitive tetragonal units consisting of a central Ti atom covalently linked to six O atoms (**Figure 2.1a**). These units are interconnected by corresponding O atoms. As such, a distinct octahedral TiO_6 unit is observed centrally; this conformation primarily forms the fundamental motif of rutile, as illustrated in **Figure 2.1b**.

The global consumption of TiO_2 from 2016 onwards is estimated at 6.1 million metric tons, and by 2025 is expected to rise to 8.83 million metric tons, due to the widespread applications of TiO_2 as engineered nanomaterials (ENMs) (Loosli *et al.* 2019). UV blocking agents, particularly those found in sunscreens, offer consumers smooth application, a clear appearance and most importantly broad-spectrum UV protection (Lewicka *et al.* 2013), leading to these agents containing nanoparticles to be categorized as the highest priority for future research (Labille *et al.* 2010). However, the advent of modern-day molecular modelling techniques has improved our understanding of the intrinsic properties of molecules that protect against the detrimental effects of the sun's rays, thus contributing to the development of more effective sunscreens. Walters and co-workers had already demonstrated that computational chemistry methodologies could correctly show the absorption spectrum of certain commercial sunscreens (Walters *et al.* 1997).

In terms of on the sizing terminology, the EC Recommendation on the definition of a "nanomaterial" (2011/696/EU) defines it as a naturally occurring, incidental or manufactured material containing particles with one or more external dimensions in the 1 – 100 nm size range. The recommendation further proceeds to describe a "nanoparticle" as a "minute piece of matter with defined physical boundaries" within the above-mentioned nanoscopic scale.

With regards to the identification of nanomaterials in complex matrices, the number of unanswered questions on the long and short-term behaviour in humans and the environment

has increased concerns of both consumers and scientists alike. However, this has inadvertently led to a lack of transparency in institutional documents and commercial communications, highlighting the need for better consumer awareness in nanotechnology and its applications (Dudefoi *et al.* 2018; Baranowska-Wójcik *et al.* 2020). Hence, there is an increasing need for methodologies able to effectively and efficiently separate nanoparticles present in complex matrices and determine the physicochemical properties of ENMs. This is critical for supporting safety assessments, for quality control of existing products, and the identification of test materials before toxicological assessments as underlined by the International Organisation for Standardisation (ISO/TR13014) (Lu *et al.* 2015; Bocca *et al.* 2018; Lim, Bae and Fong 2018). It has been suggested that nanoparticles may be more toxic than larger particles of the same chemical compound because of their enhanced chemical reactivity, larger surface area and easier cellular penetration (Tucci *et al.* 2013). Athinarayanan *et al.* (2015) reported that these particles may cause cell mitochondrial membrane damage, leading to other chronic diseases such as diabetes and cancer. Furthermore, the International Agency for Research on Cancer classified TiO_2 in nanoparticulate form as a "possible carcinogen to humans" (Fiordaliso *et al.* 2018). Both workers and consumers are more likely to be exposed to nano-TiO_2 due to the increasing global production and use of TiO_2 ENMs. Specifically, workers are more vulnerable to the exposure of higher levels of TiO_2 NPs during handling and manufacturing processes (Zhao *et al.* 2018b). Upon consideration of these factors, several analytical methods have been evaluated for size characterisation and quantification of TiO_2 NPs.

The use of the DLS technique is constrained by the over-sensitivity of its analysis on complex matrices despite its quick run times (Malm and Corbett 2019). The preference for spICP-MS is seen to be inhibited by the need for high-level expertise (Zhao *et al.* 2018a). AF4-ICP-MS is primarily utilised for NP elemental quantification but with varying success (Nischwitz and

Goenaga-Infante 2012; López-Heras, Madrid and Cámara 2014; Helsper *et al.* 2016). AF4-MALS is a technique showing high potential in the physicochemical evaluation of nano-TiO_2 in cosmetics, but is currently met with various challenges; de la Calle *et al.* (2018) highlighted the lack of TiO_2 NP standards available for AF4 analysis; Müller *et al.* (2018) employed inverse supercritical CO_2 extraction as a matrix simplifier in sample preparation, but the subsequent formation of organic acids led to TiO_2 NP instability and aggregation in sunscreen matrices during analysis; while surfactant-assisted particle extraction trialled by Velimirovic *et al.* (2020b) revealed difficulties in large particle retention in the AF4 channel during the focusing step.

In South Africa, there are currently no requirements regarding local markets for manufacturers to declare nano-enabled products (Moeta *et al.* 2019). This work, therefore, provides an exploration of the impact of PEG-TiO_2 NPs for nano-TiO_2 sunscreen analysis. In addition, the developed method can contribute to the enhanced separation and sizing of TiO_2 NPs in complex cosmetic matrices. By aligning the findings of key physicochemical parameters, the study can also contribute to physiological nanotoxicology evaluations, a key component for cosmetic nanomaterial regulatory analysis.

2.2) Nanoscale synthetic amorphous silica in processed foods

Synthetic amorphous silica (SiO_2) is one of the most highly produced and commercially used NMs worldwide (Bartczak *et al.* 2018); an anti-caking additive (E551) used in the food industry for decades (Barahona *et al.* 2016). SiO_2 occurs in two major forms, namely crystalline and amorphous, with the latter preferred in foods (Winkler, Suter and Naegeli 2016; Winkler *et al.* 2017).

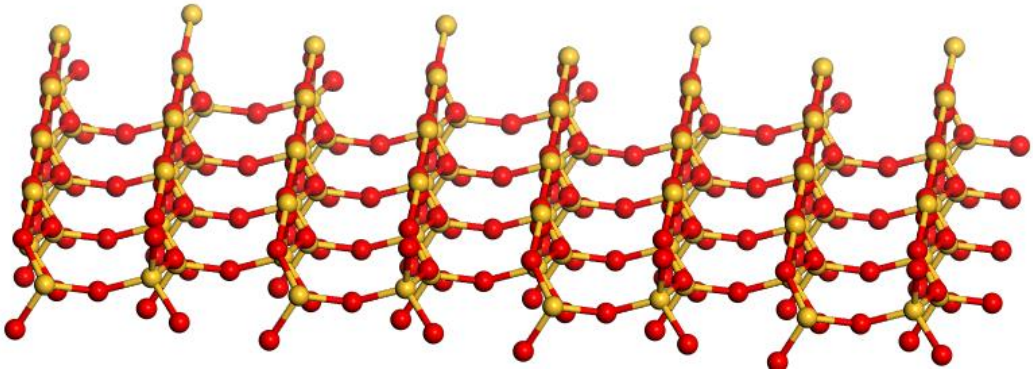

Figure 2.2. Layered structure of amorphous silica (SiO_2). The Si and O atoms are denoted in yellow and red respectively. (The 3D structures for this study were generated using MS).

Figure 2.2 illustrates the fundamental motif of SiO_2, constituted by the SiO_4 tetrahedron: a tetra-coordinated silicon atom, located at the centre, covalently linked to four oxygen atoms. The whole silica structure is then generated by the interconnection of these units, so that each oxygen atom is connected to two silicon atoms, resulting in the net chemical formula SiO_2. The global production of nanoparticulate SiO_2 is estimated at 3 million tons per year (Giese *et al.* 2018). As a result of the difference in chemical behaviour between larger and smaller particles, ENMs have gained notoriety due to possible health concerns regarding human health (Tucci *et al.* 2013). The presence of SiO_2 NPs is known to cause antioxidant enzyme secretion as well as oxidative stress due to an alteration in the human fibroblast cell, which may lead to diabetes and cancer (Athinarayanan *et al.* 2015; Zulfah and Siripinyanond 2018).

Coffee creamers with long shelf lives, a fresh-like taste and storage convenience have added to their popularity as milk or cream substitutes in coffee (Hedayatnia *et al.* 2016). Glucose in the form of corn syrup solids may constitute up to 65% of the total creamer composition (Hirpara and Jana 2011), which naturally poses the question of its interaction as a major constituent with nanosized SiO_2 present in the E551 anticaking agent.

In analytical chemistry, a solid approach in the development and treatment of the analytical data process paves the way for secure method development and validation protocols. In line

with the enhancement of the overall analytical procedure, a significant role is played by experimental design (Tauler, Kowalski and Fleming 1993; Kanchi *et al.* 2017). The conventional optimization process involves univariate analysis, or "changing-one-factor-at-a-time" approach, which increases the number of experimental runs, inflates experimental costs and is overall time-consuming. More critically, interactions between independent variables are neglected, resulting in inaccuracies of the subsequent optimized conditions of an experiment (Tayeb, Tony and Mansour 2018; Tetteh, Naidoo and Rathilal 2019). Hence, multivariate analysis has been viewed to overcome these challenges, with response surface methodology (RSM) deemed suitable. RSM, as defined by Tayeb, Tony and Mansour (2018), is a set of mathematical and statistical techniques to establish an experimental design model. The two most commonly applied experimental designs are the central composite design (CCD) and the Box-Behnken design (BBD), with the latter being comparatively more efficient (Hanrahan and Lu 2006). The main difference between the two designs is that the CCD generates data from the corner points of its orthogonal matrix, while the BBD uses the middle points of its edges (Ferreira *et al.* 2007; Willden and Jensen 2020). Consequently, the BBD avoids predicting extreme responses which would otherwise be deemed experimentally unfeasible by employing a fractional or incomplete factorial subset. The rotatability (or near rotatability) of the design ensures a symmetrical generation of responses within the experimental domain as pre-scaled by the experimenter. Lastly, the three-level requirement per factor results in fewer trial runs allowing for a more convenient and less costly optimization protocol (Box and Behnken 1960; Wu *et al.* 2012).

Most analytical studies for the size analysis of SiO_2 NPs include techniques such as dynamic light scattering, transmission electron microscopy (Barahona *et al.* 2015), nanoparticle tracking analysis, tuneable resistive pulse sensing (Bartczak, Vincent and Goenaga-Infante

2015), energy dispersive X-ray analysis (Heroult *et al.* 2014), scanning electron microscopy, centrifugal field-flow fractionation (Contado, Ravani and Passarella 2013), asymmetric flow field-flow fractionation (Bantz *et al.* 2014) and single particle inductively coupled plasma-mass spectrometry (Bolea-Fernandez *et al.* 2017). Individually used, each has its setbacks such as limited detection limits, high background interference and long analysis times. Other notable drawbacks include the large particle polydispersity bias noted as per the DLS response, along with high cost and time-consuming investigations encountered using electron microscopy (Hagendorfer *et al.* 2012). Instrumental coupling such as that of AF4 to ICP-MS has also been implemented however, only mixed levels of proficiency have been achieved (Heroult *et al.* 2014; Aureli *et al.* 2015; Barahona *et al.* 2016).

To the best of the author's knowledge, Monte Carlo simulations have not been undertaken to evaluate intrinsic interactions between SiO_2 NPs and glucose in aqueous media. As such, in this work, these computational methods together with AF4-MALS-DLS is viewed to solve the analytical problem of nano-SiO_2 analysis in complex food matrices.

CHAPTER 3 - THEORETICAL PRINCIPLES

This chapter focuses on the theoretical principles involving the experimental and computational studies. The analytical techniques discussed in this section are AF4, MALS, DLS and spICP-MS. This is followed by the theoretical principles of the Monte Carlo (MC) simulations from a computational chemistry perspective.

3.1) Experimental principles

3.1.1) Asymmetric Flow Field-Flow Fractionation (AF4)

Field-flow fractionation (FFF) was first introduced in 1966 as conceptualized by J. Calvin Giddings (Giddings 1966). It is a quasi-chromatographic method characterized by a single liquid phase separation induced by an external field applied to that of the direction of sample flow perpendicularly through a thin, flat (ribbon-like) channel (Messaud *et al.* 2009). There are several types of these techniques available, including sedimentation FFF, flow FFF, thermal FFF and electrical FFF (Takeuchi *et al.* 2009). As a result, applications occur in various fields such as environmental chemistry, polymer technology, biopharmaceutics, pharmaceutics and biotechnology (Dubascoux *et al.* 2008). The most popular and commercialized FFF method for simultaneous NP separation and size determination (Contado 2017), asymmetric flow field-flow fractionation (AF4) is a subset technique derived from the flow FFF family and is used in this work.

The separation takes place in the channel, which consists of porous and non-porous plates clamped together with a thin spacer in between (**Figure 3.1**). The porous plate constitutes a membrane supported by a frit, collectively termed the accumulation wall. The sample enters through the tip of the channel carried by a continuous flow of solvent, known as the tip flow. This stream makes up the parabolic longitudinal channel flow and the perpendicular crossflow (**Figure 3.2**). The latter is induced as a result of the tip flow channelling through the permeable

accumulation wall. Against the channel flow, a counterflow of solvent (known as the focus flow) is introduced (as an additional split of the tip flow) to focus the sample, promoting a reduction of peak band broadening and an increase in signal resolution; this is known as the focus or relaxation step. Simultaneously, the crossflow pushes sample particles towards the accumulation wall. Once there, diffusion together with the strength of the crossflow partition the particles with respect to size and density. The focus flow is then turned off and the assorted sample species proceeds through the channel. The characteristic laminar profile of the channel flow ensures that minute differences in particles are amplified as smaller particles are carried away by the central parabolic high-velocity streamlines and hence are eluted first, followed by the larger and heavier particles slowly forced along by the low-velocity streamlines at the accumulation wall. Ultimately, sample particles are separated by hydrodynamic diameter and are ascendingly eluted.

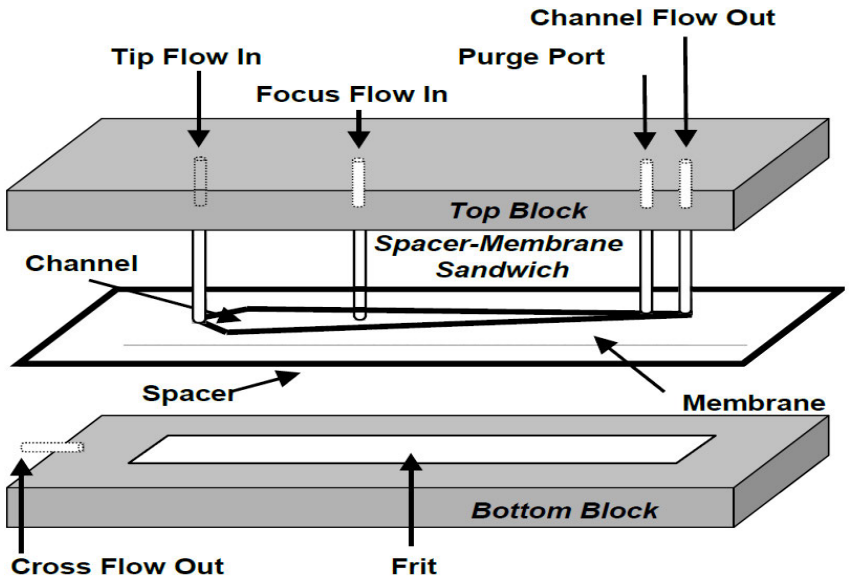

Figure 3.1. Schematics of AF4 channel, reproduced with permission from Postnova Analytics GmbH, Germany (Postnova 2016).

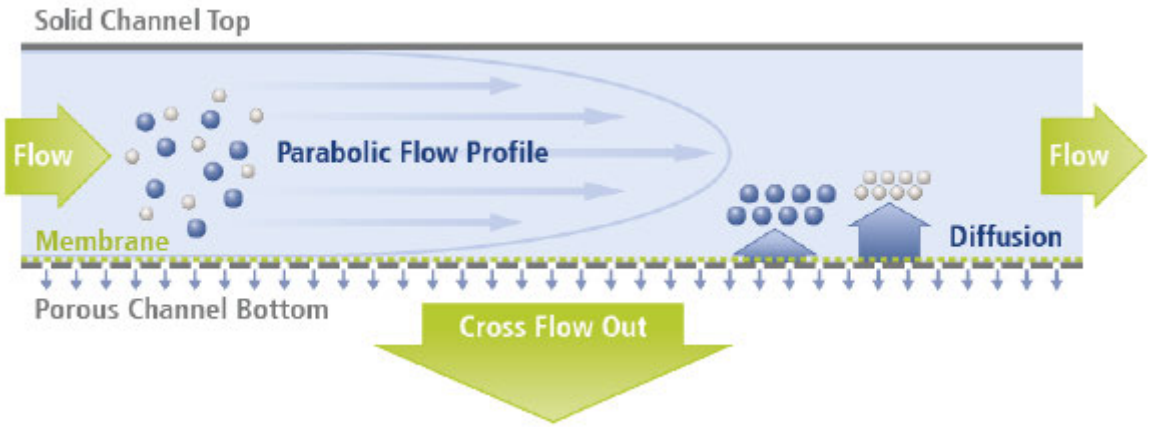

Figure 3.2. Working principle of AF4 separation, reproduced with permission from Postnova Analytics GmbH, Germany (Postnova 2017).

The following relationship is obtained for the crossflow velocity U in the x-direction (Wahlund and Giddings 1987; Cölfen and Antonietti 2000):

$$U = -|u_0|\left(1 - \frac{3x^2}{w^2} + \frac{2x^3}{w^3}\right) \tag{3.1}$$

where $|u_0|$ is the crossflow velocity at the accumulation wall, x the distance from the accumulation wall in the x-direction and w the channel width or thickness.

In a trapezoidal channel, assuming a constant crossflow, the average flow velocity in the z-direction $< v >$ is expressed by:

$$< v >= \frac{\dot{V}_{in} - |u_0|A(z)}{wb(z)} \tag{3.2}$$

where z is the direction of the carrier flow, $\dot{V}_{in}$ the flowrate at the channel inlet, $A(z)$ the accumulation wall area from the inlet up to z, and $b(z)$ the channel width at z.

In order to calculate the retention ratio R, the void time t_0 is required, given by:

$$t_0 = \frac{V_0}{\dot{V}_c} \ln\left(1 + \frac{\dot{V}_c}{\dot{V}_{out}}\left[1 - \frac{A(z') - y}{A_{tot}}\right]\right) \tag{3.3}$$

where V_0 is the void volume, $\dot{V}_c$ the crossflow rate, $\dot{V}_{out}$ the outlet flow rate, $A(z')$ the area from the inlet to the focusing point, A_{tot} the total area of the accumulation wall and y the area excluded by the tapered inlet end.

The retention parameter for asymmetric channels is given by:

$$\lambda = \frac{DV_0}{\dot{V}_c w^2} \tag{3.4}$$

For conditions pertaining to sufficiently high retention, a relationship between λ and R can be deduced by simple approximation in the form $R = 6\lambda$.

If $R = 6\lambda$ is assumed, **Eq. (3.4)** can be expressed as:

$$t_r = \frac{t_0 \dot{V}_c w^2}{6DV_0} \tag{3.5}$$

which allows for the absolute direct determination of the diffusion coefficient D by measurement of t_r. Assuming $R = 6\lambda$, the combination of the Stokes-Einstein relationship with **Eq. (3.4)** expresses the relation of t_r to the hydrodynamic diameter D_H:

$$D_H = \frac{2kTV_0}{\pi\eta \dot{V}_c w^2 t_0} t_r \tag{3.6}$$

3.1.2) Multi-Angle Light Scattering (MALS)

The earliest implementations of MALS involved polystyrene light scattering investigations conducted by Bruno H. Zimm (Zimm 1948). The principle entails the measuring of light scattered by sample particles at multiple angles, relative to an incoming laser beam, for the determination of particle size and molar mass (Lohrke, Briel and Mäder 2008). It is a technique used not only in biological and biopharmaceutical sciences, but in all those fields in which "polymers" are involved for particle and macromolecule characterization.

Essentially, a laser beam illuminates a given sample (**Figure 3.3**). The electric field of the laser transcends that of the electron clouds in terms of electronic shell swings of each atom in the sample by means of identical incident light frequency. The respective atoms ultimately act as isotropic light scattering sources, the intensities of which are determined by multiple surrounding detectors situated at different angles (**Figure 3.4**). Two deductions are clear; firstly, the scattered light intensity is proportional to the product of the concentration and molar mass of the sample; and secondly, while smaller particles scatter light isotropically with the same intensity, larger particles scatter light primarily in a forward direction.

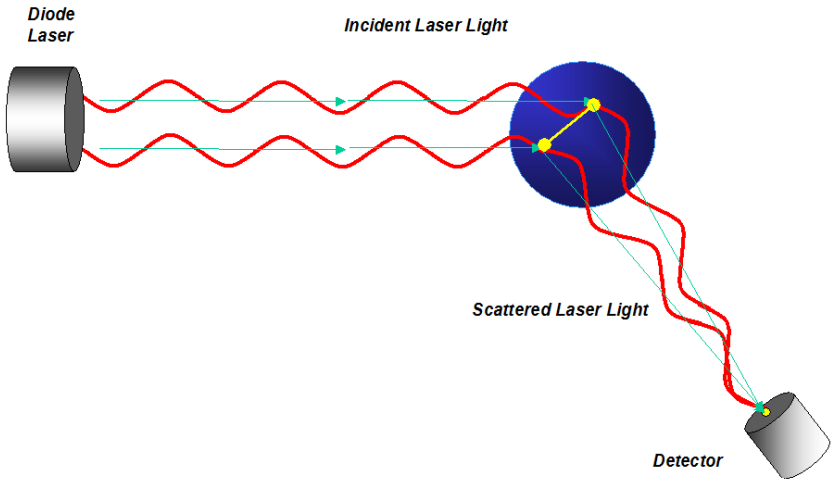

Figure 3.3. Schematics of MALS detector, reproduced with permission from Postnova Analytics GmbH, Germany (Postnova 2017).

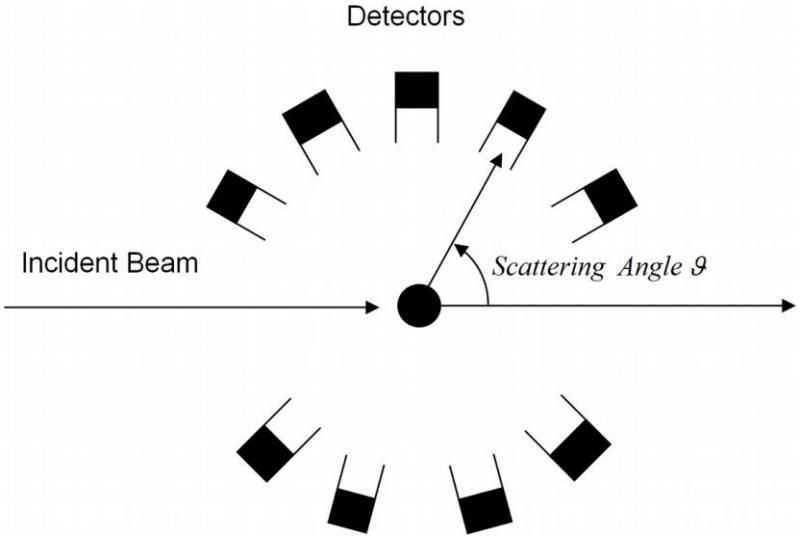

Figure 3.4. Light scattering principle of MALS detector, reproduced with permission from Postnova Analytics GmbH, Germany (Postnova 2017).

For a homogenous sphere of radius a, the angular dependency of scattered light per unit solid angle per unit intensity for incident vertically polarized light of intensity I_0, may be expressed as (Wyatt 2014):

$$\frac{I}{I_0} = \frac{(ka)^4 V^2}{4\pi} |m-1|^2 \left[G\left(2x \sin\frac{\theta}{2}\right)\right]^2 \tag{3.7}$$

$$= \frac{(ka)^4 V^2}{4\pi} |m-1|^2 P(\theta)$$

where $V = (\frac{4}{3})\pi a^3$. As such, the function $G(u)$ is written as:

$$G(u) = \frac{3}{u^3}(\sin u - u\cos u) \tag{3.8}$$

and thus, by deduction, the form factor or particle scattering function $P(\theta)$ is given by:

$$P(\theta) = \left(\frac{3}{u^3}(\sin u - u\cos u)\right)^2 \tag{3.9}$$

The relation of $P(\theta)$ to $R(\theta)$

From the general turbidity τ of a solution, an expression in relation to the excess Rayleigh ratio $R(\theta)$ is defined:

$$\tau = \frac{16\pi}{3} R(\theta) \tag{3.10}$$

Pertaining to Zimm for vertically polarized incident light (laser) of fixed wavelength at extremely dilute concentrations, **Eq. (3.7)** becomes:

$$\frac{R(\theta)}{(K^* c)} = MP(\theta) \tag{3.11}$$

where $K^* c$ is the contrast factor, M the molar mass and $P(\theta)$ the general form factor.

The determination of particle size using radius of gyration (r_g)

A generic description of a particle's centre of gravity can be used to obtain a convenient measure of the average square of the distance from this centre (r_i^2) to each mass element (m_i) of the particle. Derived from measurements of the light scattered by a monodispersed suspension of such particles, by Rayleigh-Gans approximation we obtain the mean square radius $\langle r_g^2 \rangle$:

$$\langle r_g^2 \rangle = \frac{\sum_i m_i r_i^2}{\sum_i m_i} \tag{3.12}$$

If the particle density ρ is homogeneous, the expression becomes:

$$\langle r_g^2 \rangle = \frac{\sum m_i r_i^2}{M} = \frac{\sum v_i r_i^2}{V} = \frac{1}{V} \iiint R^2(r, \theta, \varphi)\, dv \tag{3.13}$$

where the total particle volume is V, $M = \rho V$, $m_i = \rho v_i$, and $R(r, \theta, \varphi)$ is the distance of the mass element ρdv from the particle centre of mass. For a homogenous sphere of radius a, **Eq. (3.13)** yields:

$$\langle r_g^2 \rangle = \frac{1}{V} \iiint r^2 dV = \frac{3}{4\pi a^3} \int_0^{2\pi} d\varphi \int_0^{\pi} \sin\theta \, d\theta \int_0^{a} r^4 dr = \frac{3}{5} a^2 \tag{3.14}$$

From the square root of the mean square radius, the radius of gyration (r_g) is obtained:

$$r_g = \sqrt{\frac{3}{5}} a \tag{3.15}$$

Furthermore, by considering the natural geometry of real-life particles in comparison to that of the perfect theoretical spherical model, the following relation is expressed:

$$D_{geo} = \frac{r_g}{\sqrt{\frac{3}{5}}} \times 2 \tag{3.16}$$

where D_{geo} is the geometric diameter and r_g is determinable from the MALS detector at 90°.

The relation of r_g to $P(\theta)$

To illustrate the relation between r_g and $P(\theta)$, we start by introducing the generic theoretical homogenous particle mean square radius $\langle r_g^2 \rangle$ as per Wyatt (2018) by the alternate equation:

$$\langle r_g^2 \rangle = \frac{1}{2n^2} \sum_{i=1}^{n} \sum_{j=1}^{n} \langle h_{ij}^2 \rangle \tag{3.17}$$

where h_{ij} is the distance between the i^{th} and j^{th} mass element and $\langle h_{ij}^2 \rangle$ is the square of this distance averaged over all conformations.

Furthermore, we can express the form factor as:

$$P(\theta) = \frac{1}{n^2} \sum_{i=1}^{n} \sum_{j=1}^{n} \frac{\sin \mu h_{ij}}{\mu h_{ij}} = \frac{1}{n^2} \sum_{i=1} \sum_{j=1} \left[1 - \frac{(\mu h_{ij})^2}{3!} + \frac{(\mu h_{ij})^4}{5!} \ldots \right], \tag{3.18}$$

where $\mu = \frac{4\pi}{\lambda} \sin \frac{\theta}{2}$. We can rewrite **Eq. (3.18)** from **Eq. (3.17)** to obtain:

$$P(\theta) = 1 - \frac{\mu^2}{3 \cdot 2 \cdot n^2} \sum_{i=1}^{n} \sum_{j=1}^{n} \left(h_{ij}^2\right) + \frac{\mu^4}{5 \cdot 4 \cdot 3 \cdot 2 \cdot n^2} \sum_{i=1}^{n} \sum_{j=1}^{n} \left(h_{ij}^4\right) \ldots \tag{3.19}$$

$$= 1 - \frac{\mu^2}{3} \langle r_g^2 \rangle + \frac{\mu^4}{5 \cdot 4 \cdot 3 \cdot 2 \cdot n^2} \sum_{i=1}^{n} \sum_{j=1}^{n} \left(h_{ij}^4\right) \ldots$$

where $\mu^2 = \frac{16\pi^2}{\lambda^2} sin^2(\theta/2) = \frac{16\pi^2}{\lambda^2} \xi$. With respect to ξ, where $\xi = sin^2(\theta/2)$, differentiating **Eq. (3.19)** yields:

$$\langle r_g^2 \rangle = \frac{-dP(\theta)}{d\xi} \left(\frac{3\lambda^2}{16\pi^2} \right) + terms\ \alpha\ \xi^2, \xi^4, \ldots \tag{3.20}$$

and further limiting **Eq. (3.20)** to the initial slope of $P(\theta)$, i.e., $\lim_{\xi \to 0} \left(\frac{dP(\theta)}{d\xi} \right)$, we finally obtain:

$$\langle r_g^2 \rangle = \left(\frac{3\lambda^2}{16\pi^2} \right) \lim_{\xi \to 0} \left(\frac{-dP(\theta)}{d\xi} \right) \tag{3.21}$$

3.1.3) Dynamic Light Scattering (DLS)

Dynamic light scattering (DLS), otherwise known as photon correlation spectroscopy (PCS) or quasi-elastic light scattering (QELS), is a technique that primarily measures the Brownian motion of particles and macromolecules in solution that occurs due to solvent molecule bombardment, and correlates this motion for particle size determination (Stetefeld, McKenna and Patel 2016). It has numerous applications in important sectors such as medicine, manufacturing, food, environmental and biopharmaceutical sciences (Malm and Corbett 2019).

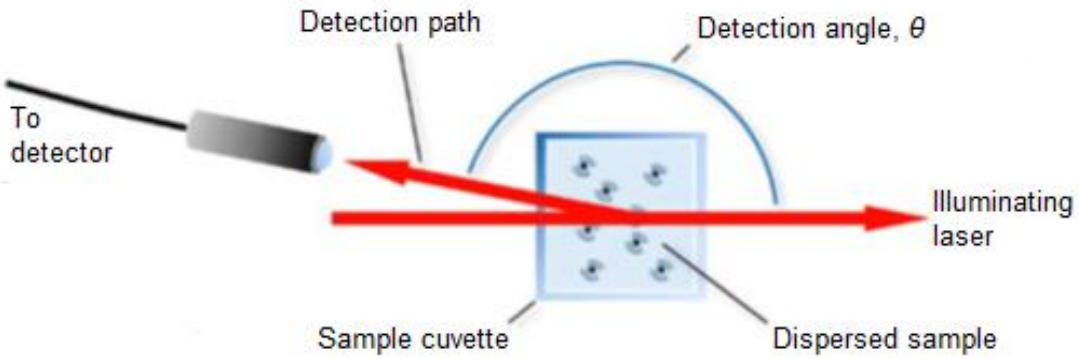

Figure 3.5. Schematics of DLS detector, reproduced with permission from Malm and Corbett (2019).

The detection path from the cuvette to the detector with an illuminating laser (**Figure 3.5**) is described by the $\boldsymbol{q}$-vector (Malm and Corbett 2019):

$$|\boldsymbol{q}| = \frac{4\pi n}{\lambda} \sin\left(\frac{\theta}{2}\right) \tag{3.22}$$

where λ is the wavelength of the laser in air, n the dispersion liquid phase refractive index and θ the free-space angle between the laser and detection path.

The Rayleigh scattering model incorporates the light scattered from a given particle in terms of the scattered intensity, I:

$$I \propto \frac{r^6}{\lambda^4} \tag{3.23}$$

which is proportional to the sixth power of the particle radius r, for fixed wavelength λ.

Subsequently, from the detector, the scattered photon time-series $I(t)$ is deduced from the measured autocorrelation function $g^2(|\boldsymbol{q}|;\tau)$, given by:

$$g^2(|\boldsymbol{q}|;\tau) = \frac{\langle I(t)I(t+\tau)\rangle}{\langle I(t)\rangle^2} \tag{3.24}$$

where τ is the delay time, and I the measured detector intensity in photon counts per second at time t. We obtain g^1, the first-order correlation function, via the Siegert relation with a cumulants-fit such that:

$$g^1(|\boldsymbol{q}|;\tau) = exp\left(-\bar{\Gamma}\left(\tau - \frac{\mu_2}{2!}\tau^2 + \frac{\mu_3}{3!}\tau^3 + \cdots\right)\right) \tag{3.25}$$

where $\bar{\Gamma}$ is the average decay rate in a given sample and $\mu_2/\bar{\Gamma}^2$ is the 2nd order polydispersity index (PDI). The z-average diffusion coefficient, D_z, is then given by the relation:

$$\bar{\Gamma} = |\boldsymbol{q}|^2 D_z \tag{3.26}$$

From **Eq. (3.26)**, using the Stokes-Einstein model for spherical particles in liquids with low Reynolds number, we yield an expression for the average hydrodynamic diameter, D_H:

$$D_H = \frac{k_B T}{3\pi\eta D_z} \tag{3.27}$$

where k_B is the Boltzmann constant, η the dispersant viscosity and T the absolute temperature of the dispersant.

3.1.4) Single Particle Inductively Coupled Plasma-Mass Spectrometry (spICP-MS)

The first commercially available ICP-MS instrument was introduced in 1983 (Olesik 1991). Since then, the technique has been diversely deployed in numerous fields such as environmental and life sciences, food, geochemistry, archaeology and forensics (Ammann 2007). Widely employed for the determination of trace elements at very low concentrations, it combines high sensitivity with multiple advantages such as broad elemental coverage, wide linear dynamic range, high sample throughput and simple sample preparation (Wilschefski and Baxter 2019). Recently, spICP-MS has surged in interest where it has proven to be a powerful

technique for the detection and size characterization of ENMs in aqueous dispersions (Montaño *et al.* 2016). The work in this project focuses on colloidal nanodispersion analysis. The sample is introduced in aerosol form via the nebulizer, following which the analyte desolvates, atomizes and ionizes in contact with the argon based high-temperature plasma (**Figure 3.6**). The target ions are then extracted from the plasma interface and separated under vacuum by the mass spectrometer using the particles' mass to charge ratio (m/z). The instrument detects charges of particles equivalent to one, thus m/z is taken as identical to the atomic mass of the particle analyzed. In spICP-MS, this is considered a signal pulse event. An electron multiplier detector then counts the ions after which results are obtained and interpreted on the data management software.

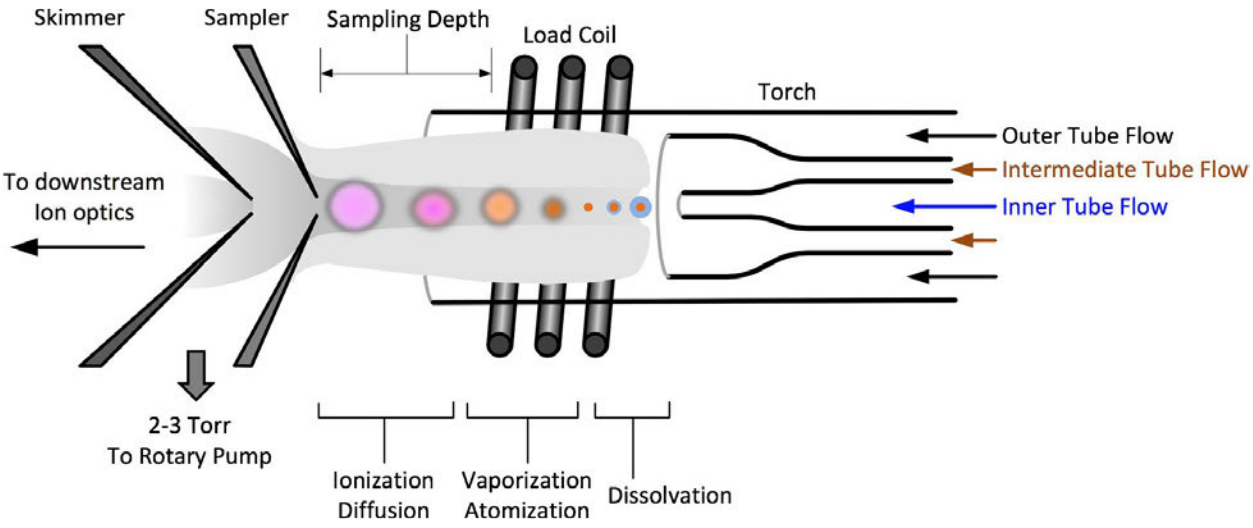

Figure 3.6. Aerosol desolvation, atomization and ionization in plasma, reproduced with permission from Montaño *et al.* (2016).

The crux of the technique is dependent on the pulse signal intensity, I_p, and its relationship with the analyte concentration, c (Pace *et al.* 2011; Kim *et al.* 2013):

$$I_p \propto c \tag{3.28}$$

Considering spICP-MS experimental factors, c is given by:

$$c = \frac{m}{q_{col} t_{dt} \eta_{neb}} \tag{3.29}$$

where m is the mass observed per event, q_{col} the nanoparticular colloidal sample flow rate, t_{dt} the dwell time and η_{neb} the nebulizer transport efficiency.

The above-mentioned individual pulse signal intensity (I_p) after subtraction of the average background intensity, I_{Bgd}, can be incorporated to deduce the mass of a corresponding particle, m_p, following integration into the calibration curve function below:

$$m_p = f_a^{-1}\left[\frac{\left(\left(I_p - I_{Bgd}\right)/\eta_i\right)}{m_{cal}}\right] \tag{3.30}$$

where f_a is the mass fraction of the analysed element in the particle, η_i the particle ionization efficiency and m_{cal} the slope of the calibration curve.

Assuming a spherical particle model fit, the diameter, d, can be obtained by:

$$d = \left(\frac{6m_p}{\pi\rho}\right)^{\frac{1}{3}} \tag{3.31}$$

where ρ is the particle density.

3.2) Computational modelling

3.2.1) Monte Carlo (MC) simulation

The original paper describing Monte Carlo (MC) simulations in molecular chemistry was published in 1953 (Metropolis *et al.* 1953). The overall procedure involves building individual molecules or particles of interest by stipulated computer software and allowing them to interact via computer simulation with respect to predetermined thermodynamic equilibrium conditions.

Energy calculations are then performed to determine the state of interparticle interactions together with the overall stability of the designated system. A key endeavour in this project is to synergise the results of the experimental studies to that of the computational findings to provide a compelling picture into the intrinsic nanoparticle interaction phenomena of this work. The premise of the method focuses on the establishment of predefined thermodynamic conditions in a canonical ensemble, which can be defined as a statistical ensemble of systems in configurational space governed by a thermal reservoir constantly yet gradually distributing an infinitive amount of heat through the respective system. The idea behind this experiment is to provide a medium by which particles within the ensemble are individually allowed to move, specifically by means of thermal equilibrium – this ambience corresponds to the laboratory environment equilibrated conditions. One must also consider that for the original MC algorithm, there are no restrictions on ranges of density or temperature.

In a devised system, we consider a finite N number of particles in subsequent periodic supercells aligned in the same configuration in each unit cell; this periodicity of cells is representative of a complete substance surface. We acknowledge that the potential occurring between the closest distance between two particles withholds the greatest relative energetic contribution in comparison to other interparticle distances. If the positions of the N particles are known in each cell, we can determine the potential energy of the system:

$$E = \frac{1}{2} \sum_{\substack{i=1 \\ i \neq j}}^{N} \sum_{j=1}^{N} V(d_{ij}) \tag{3.32}$$

where V is the potential between particles i and j, with d_{ij} the minimum distance between them.

We can evaluate the properties of the system by using the aforementioned canonical ensemble in terms of the equilibrium value of any quantity of interest F, by the equation below:

$$\bar{F} = \left[\int F \exp(-E/kT) d^{2N}p d^{2N}q\right] \Big/ \left[\int \exp(-E/kT) d^{2N}p d^{2N}q\right] \tag{3.33}$$

where $d^{2N}p d^{2N}q$ is the volume element of the equation, and $\exp(-E/kT)$ acts as a weighting function with k the Boltzmann constant and T the absolute temperature.

We begin the algorithm by first successively moving each of the particles according to the following prescription:

$$\begin{aligned} X &\rightarrow X + \alpha\xi_1 \\ Y &\rightarrow Y + \alpha\xi_2 \end{aligned} \tag{3.34}$$

where α is the maximum allowed displacement, and ξ_1 and ξ_2 random numbers between -1 and 1. The ξ values play an imperious role in determining the actual translocation limits of a particle in relation to its neighbour, while still concurring with the arbitrary value of α. The property $\exp(-E/kT)$, from **Eq. (3.33)**, can be viewed as a potential state of existence by weight for a prospectively shifted particle, coinciding with the spatial constrictions of the above prescription. We choose a probability of $\exp(-E/kT)$ having small values (thus low weight) by selecting close-packed configurations and weighting them evenly.

To further elaborate, we return to our algorithm, where we let one particle move as per **Eq. (3.34)**. We then calculate ΔE, the change in energy of the system, as a result of the move. If $\Delta E < 0$ - meaning the move stabilises the system i.e. brings the system to a lower state of energy - we allow the move, with the particle then placed in its new position. If $\Delta E > 0$, we choose a probability $\exp(-E/kT)$ as stated above by selecting a random number ξ_3 between 0 and 1, and if $\xi_3 < \exp(-E/kT)$, we allow the particle to move to its new position. If $\xi_3 > \exp(-E/kT)$, the particle remains in its original position. Subsequently, whether the move is

allowed or not (whether we are in a different configuration or the original configuration), we take it that we are in a new configuration so as to obtain our averages. Thus, we have the equation:

$$\bar{F} = (1/M)\sum_{j=1}^{M} F_j \tag{3.35}$$

where M is the moved population of N particles and F_j is the value of the property F of the system after the j^{th} move is carried out as per the complete prescription above. After attempting to move a particle, we proceed similarly with the next one. Finally, the mathematical Monte Carlo computation is incorporated by determining the integrals pertaining to the high number of designated particles over random sets of data points. This is done in lieu of manual integration of a regular array of points, which may prove impractical judging by the immense scale of the calculations.

CHAPTER 4

Case Study I – Investigation of TiO_2 nanoscale ingredients in sunscreens by AF4-MALS-DLS and spICP-MS supported by computational modelling

In the present study, commercially available nanoparticles comprised of anatase TiO_2 were capped with poly(ethylene glycol) (PEG) to reduce the aggregation of the NPs in dispersion media. Accordingly, this prompted the need to incorporate computer simulations to assess the best adsorption site of PEG onto different locations on the anatase TiO_2 nanoclusters. On the other hand, the separation and size characterisation of PEG-TiO_2 NPs were performed using AF4-MALS-DLS, supported by spICP-MS and TEM analysis. Further characterisation was undertaken using zeta potential analysis, UV-Vis Spectroscopy, Attenuated Total Reflectance Infrared (ATR-IR) Spectroscopy and Thermogravimetric/Differential Scanning Calorimetry analysis (TGA/DSC). Finally, the performance of the developed AF4-MALS-DLS method was evaluated using two commercial SPF 50 sunscreen samples of different brands for TiO_2 NP analysis.

4.1) Experimental

4.1.1) Chemicals and reagents

All chemicals used in this study were analytical grade. Ultrapure water (18.2 MΩ cm^{-1} resistivity at ambient temperature) was prepared by a Milli-Q Advantage A10 Water Purification System (Millipore, Amsterdam, Netherlands). NovaChem Surfactant 100 solution, a special mix of ionic and nonionic detergents for FFF applications, along with a latex standard nanoparticle calibration mixture with sizes 60 nm, 125 nm and 350 nm, were purchased from Postnova Analytics (Landsberg, Germany). Dissolved standards of gold and titanium along with gold nanoparticle (AuNP) standards with particle sizes of 30, 60, and 90 nm for ICP-MS analysis were obtained from PerkinElmer (Shelton, USA). Hexane (≥ 97.0%), nitric acid (65%, Suprapur), Triton X-100, sodium dodecyl sulphate (SDS) (≥ 99.0%), potassium chloride (KCl) (≥ 99.0%) and poly(ethylene glycol) (PEG molecular weight 10 000 $g.mol^{-1}$)

were purchased from Sigma-Aldrich (Johannesburg, South Africa). Titanium dioxide anatase nanodispersion (< 100 nm) was obtained from Sisco Research Laboratories (Mumbai, India). Two commercial sunscreens, purchased in local pharmacies, were selected based on product labels and equivalent sun protection factor values (SPF 50). One sunscreen indicated the presence of nanoscale TiO_2, labelled "nano-TiO_2", while the other did not specify the scale but just stated "titanium dioxide" on the ingredients list (**Appendix 1**).

4.1.2) Capping of TiO_2 NPs with PEG

A quantity equivalent to 1 g of TiO_2 NPs was added to an aqueous mixture consisting of 0.15 g of PEG and 0.03 g of SDS in 30 ml ultrapure water. Following 1 h of continuous stirring, the solution was sonicated for 30 min using a 150 W ultrasonic bath (Labotec, Durban, South Africa). Thereafter, the sample was distilled to remove water from the mixture and subsequently heated in an oven for 12 h at 80°C to ensure complete drying. Finally, the sample was ground to obtain a fine powder. (Manorama *et al.* 2002)

4.1.3) Sample preparation of commercial sunscreens

4.1.3.1) spICP-MS

A 0.1% (w/v) suspension was made by dispersing 0.2 g of sunscreen in 1% Triton X-100 aqueous solution. A well-homogenised mixture was formed after vigorous stirring and sonication. Thereafter, a 1:5000000 dilution was made using ultrapure water and subsequently run by spICP-MS. (Dan *et al.* 2015)

4.1.3.2) AF4-MALS-DLS

Into a 50 ml plastic tube, 10 ml of hexane was added to a weighed aliquot of 0.1 g sunscreen. The mixture was shaken thoroughly, sonicated for 30 min and then allowed to settle for 1 h. After 5 min of centrifugation at 3000 rpm, the clear hexane supernatant was carefully removed by pipette. Following the addition of 20 ml of ultrapure water to the pasty white solid residue, the tube was vigorously shaken and finally sonicated for 30 min before analysis. (Nischwitz and Goenaga-Infante 2012)

4.1.4) Instrumentation

4.1.4.1) AF4-MALS

The AF4 system (model AF2000 Multiflow, Postnova Analytics) was used in this study. The MALS detector (model PN3621, Postnova Analytics) was operated at 21 different angles, with 90° preferred as optimum. The AF4 channel flow rate was kept constant at 0.5 ml/min, with the pressure not exceeding 9 bars. A 350 μm spacer was used alongside a 10 kDa molecular weight cut-off regenerated cellulose membrane as the accumulation wall. The carrier liquid used was 0.005% NovaChem 100 aqueous solution. A 0.2 mg/ml PEG-TiO_2 NP aqueous solution was prepared for optimization of the AF4 method, with the injection volume selected to be 40 μl. The focusing time was a total of 9.5 min. The optimized crossflow was 1.5 ml/min, with its exponential decay fixed at 0.2. AF4-MALS calibration was performed using a latex nanoparticle standard mixture of sizes 60 nm, 125 nm and 350 nm whereby the particle separation efficiency and size determination capabilities of the method were assessed with NovaFFF AF2000 software (version 2.1.0.4®).

4.1.4.2) AF4-DLS and zeta potential analysis

The DLS measurements were performed in Flow mode after coupling to the AF4 by quartz flow cell using the Zetasizer (Nano ZS, Malvern Instruments Ltd., UK) and its software. Zeta potential analysis was completed separately using disposable folded capillary cells in Standard mode of the instrument in 1 mM KCl solution (pH = 5.6). Measurements were performed at 25℃.

4.1.4.3) spICP-MS

Single particle ICP-MS analyses were performed on a PerkinElmer NexION 2000 ICP-MS (Perkin Elmer, Shelton, USA) operating in Standard mode. Data collection, processing and statistical analyses were performed using the Syngistix Nano Application software module. The transport efficiency was determined using 30 nm, 60 nm and 90 nm AuNP standards and dissolved 1, 2 and 5 µg/l Au standards. Dissolved Ti standard solutions of concentrations of 1, 2 and 5 µg/l were used for particle size calibration. Instrumental conditions were optimized for maximum sensitivity of Ti^{48} (ISO/TS 19590). Particle size distribution information was obtained from an automatic peak area integration of individual particles after each run using the Syngistix Nano Application module.

4.1.4.4) TEM

Morphology studies were undertaken by Transmission Electron Microscopy (TEM) with instrument model JEM 2100 equipped with a LaB_6 emitter (X-Max - Oxford Instruments). All experiments were conducted at 25℃. The measurements were undertaken using ImageJ software.

4.1.5) Spectroscopic and thermogravimetric studies

In the wavelength range of 200 – 400 nm, the Varian Cary 50 UV-Vis Spectrophotometer analysed the TiO_2 NPs, PEG and PEG-TiO_2 NPs in aqueous dispersion, while the ATR spectra were recorded from 4000 cm^{-1} to 1000 cm^{-1} on the Cary 630 FTIR Spectrometer (Agilent Technologies, Santa Clara, USA). Thermogravimetric/Differential Scanning Calorimetry analyses were performed using a TGA/DSC STAR^e system, 1 SF/1346 model with STAR^e software version 9.20 by Mettler Toledo (Johannesburg, South Africa). At a heating rate of 10℃ min^{-1}, the samples were placed in a 10 μl alumina sample holder for thermal analysis.

4.1.6) Computational modelling methodology

4.1.6.1) Titanium dioxide nanoclusters

The crystal type of TiO_2 anatase was obtained as spherical. Indeed, the anatase phase of TiO_2 was selected in the simulation based on the materials used in the experimental work. Also, this structure is generally favourable from the solution-phase methods (Zhang and F. Banfield 1998; Zaban *et al.* 2000; Oskam *et al.* 2003) as compared to other phases such as rutile. To minimize the computational cost, spherical TiO_2 anatase nanoclusters with 2 nm, 4 nm and 6 nm diameters were built conforming to the standard library of parameters of the Material Studio (MS) software package developed by BIOVIA (BIOVIA 2016b). Due to the computational time required for larger particle sizes, the aforementioned TiO_2 NPs sizes were selected for the simulation as depicted in **Figure 4.1**.

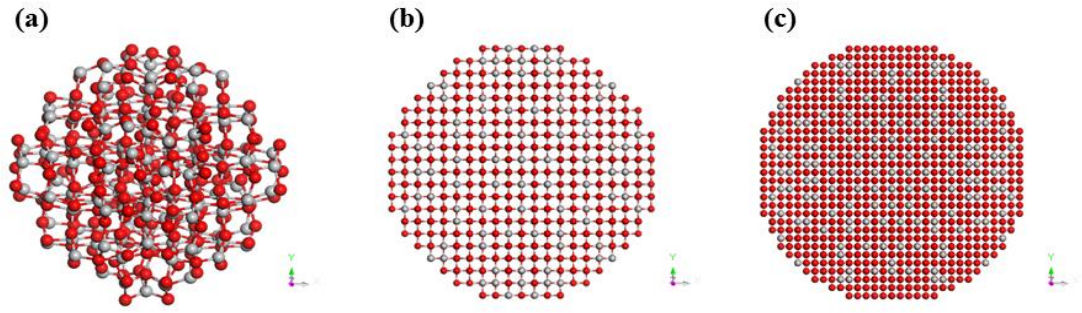

Figure 4.1. TiO_2 anatase simulated nanoparticles of sizes **(a)** 2 nm **(b)** 4 nm and **(c)** 6 nm. The Ti and O atoms are depicted in grey and red respectively. (The 3D structures for this study were generated using MS).

4.1.6.2) Poly(ethylene glycol) (PEG)

The molecular structure of PEG was constructed with monomers using the Polymer Builder module in the MS software. Forcite code was a preferable method to observe the low energy configuration (rather "most stable conformation") of PEG, along with the "ultrafine" quality of the COMPASS force-field (Sun 1998b; Sun, Ren and Fried 1998). The convergence criteria i.e. the maximum value of energy change, force, stress, and displacement were set at 2×10^{-5} kcal/mol, 0.001 kcal/mol/Å, 0.001 GPa, and 1×10^{-5} Å, respectively (Lephalala *et al.* 2020). The optimized PEG chain is shown in **Figure 4.2**.

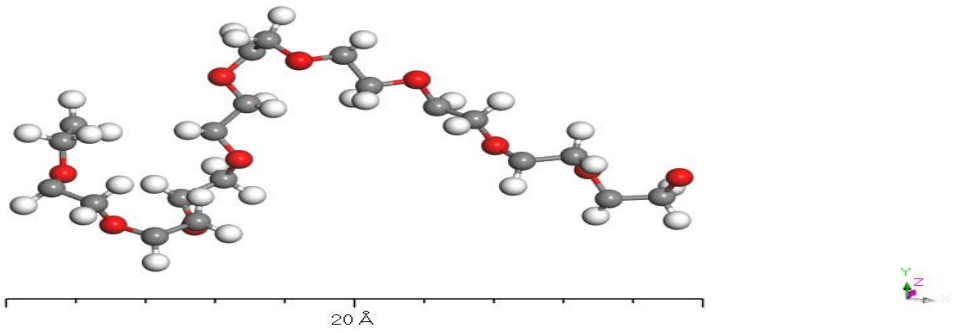

Figure 4.2. Simulated poly(ethylene glycol) chain. The C, H and O atoms are denoted in grey, white and red, respectively. (The 3D structures for this study were generated using MS).

4.1.6.3) Adsorption studies of PEG and water onto TiO_2 nanoclusters

The Adsorption Locator (AL) module in the MS software was used to obtain the best adsorption site for the PEG adsorbate onto the TiO_2 surface sites, and for comparative purposes, water molecules were used as a reference adsorbate in a separate simulation. Additionally, different ratios of the number of PEG to water molecules were simultaneously adsorbed onto the TiO_2 surface. In all cases for the initial adsorption, a UNIVERSAL force-field was applied and the charges were assigned using the QEq charge equilibrium method. The summation method for the electrostatics and the van der Waals interactions were both "atom-based" and the quality of the calculations was set to "ultra-fine". As a comparison, the simulations with larger diameters of TiO_2 were repeated to observe the adsorption energies.

4.2) Results and discussion

4.2.1) Experimental

4.2.1.1) Optimization of AF4-MALS-DLS method

While the primary focus was to analyse the commercially available nano-TiO_2 anatase dispersion, an emphasis was placed on the sample preparation of the analyte prior to the analysis. Improving and implementing an efficient sample preparation procedure for AF4 analysis has proven to be troublesome despite recent advances in current methodologies (Müller *et al.* 2018; Velimirovic *et al.* 2020a). Taking into account the instrumental protocol followed as per the methodology section, as a trial for uncapped TiO_2 NPs analysis, the fractogram in **Figure 4.3** was obtained.

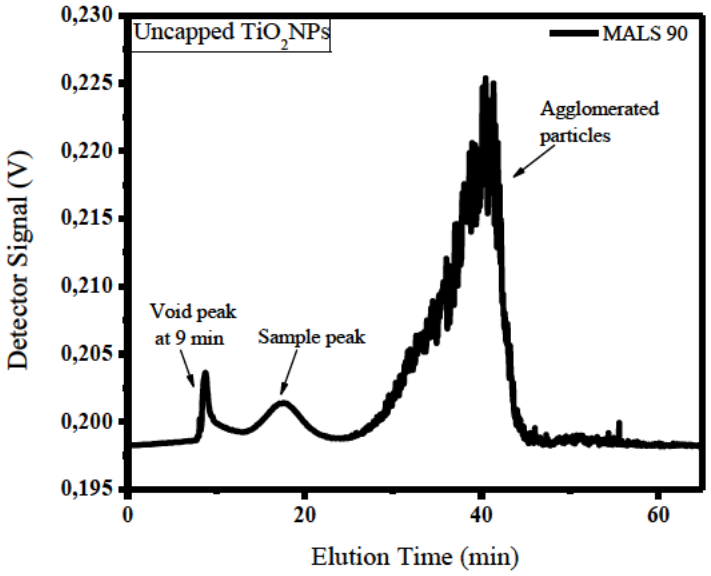

Figure 4.3. AF4-MALS fractogram of uncapped TiO_2 NP suspension.

Indeed, these appear to be non-ideal results. By inspection, however, we can deduce many key points. Firstly, the void peak signal intensity was much higher than that of the sample peak, indicative of insufficient relaxing in the focusing step. Secondly, the sample peak (at 19 min elution time) appears to be significantly suppressed, depicting poor TiO_2 retention. Also, the large secondary peak (at 40 min elution time) is undoubtedly noisy and is representative of unresolved agglomerated particles and non-ideal scattering. The aggregation of uncapped TiO_2 NPs is further highlighted by TEM analysis (**Figure 4.9a**). However, this line of "worst-case" findings allowed for the possibility of searching for another way of stabilising these particles prior to subsequent analysis.

PEG has provided optimum stabilisation of anatase TiO_2 NPs as a capping agent compared to other polymeric compounds (Manorama *et al.* 2002). Furthermore, the polymer's dispersive properties on TiO_2 have been well documented in literature (Mano *et al.* 2012; Rahim, Sasani Ghamsari and Radiman 2012; Zhang *et al.* 2016; Selli *et al.* 2019).

At first, AF4 parameters such as crossflow (V_c) and the injection volume were optimized for the high separation efficiency of the PEG-TiO_2 NPs (**Figures 4.4a-b**). For the crossflow, a

distinguishable separation between the void and sample peak was achieved after 14 mins at V_c = 1.5 ml/min, shown in **Figure 4.4a**. With respect to the other crossflows, it was noted that general peak shouldering occurred closer to the void peak. This can be represented by insufficient relaxation at those flow rates, with a focus on reducing the sample volume not so much that the PEGylated particles are pressed against the membrane during the focusing step contributing to potential channel overloading.

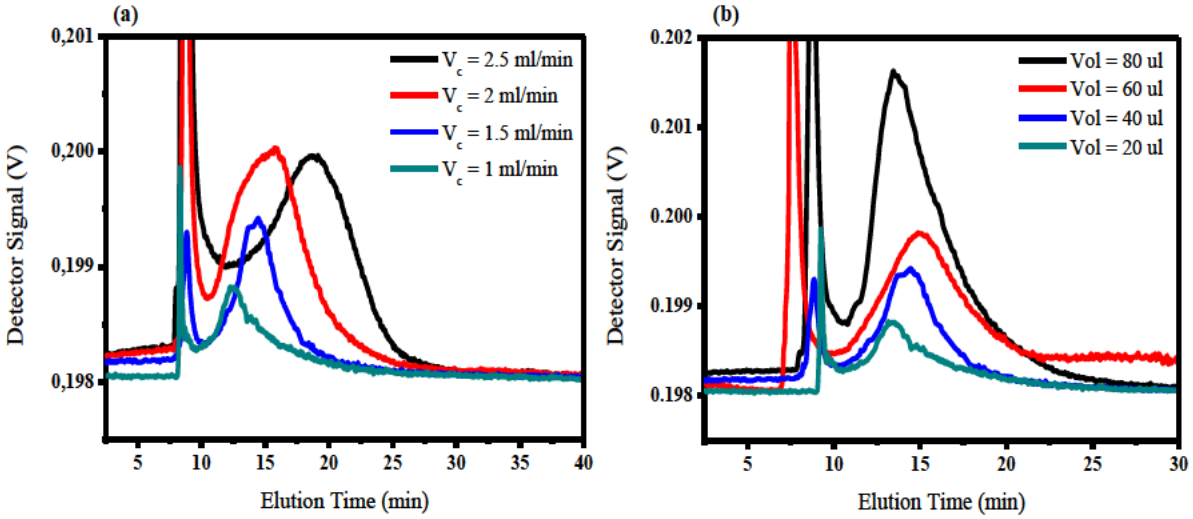

Figure 4.4. AF4-MALS fractogram overlays of 0.2 mg/ml PEG-TiO_2 NP suspension at different **(a)** crossflow rates and **(b)** injection volumes. In these fractograms, the supporting variables (injection volume in **(a)**; crossflow in **(b)**) have simultaneously been adapted to accommodate the varying variables (crossflow in **(a)**; injection volume in **(b)**) in view of possible inter-parameter interactions.

The injection volumes shown in **Figure 4.4b** depict a proportional relationship whereby increasing the injection volume increases the signal peak intensity. At 80 μl, an excess spike in signal intensity is observed, possibly due to insufficient relaxation during the focusing step. Ideally, for large volumes, a sufficiently high crossflow is required for separation. However, this could impact the long-term performance of the AF4 instrument, resulting in high particulate retention by the cellulose membrane subsequently leading to memory analyte interference and possible clogging of tubing. Thus, in addition to its optimum resolution, an injection volume of 40 μl was selected.

4.2.1.2) Size characterisation and distribution of PEG-TiO_2 NPs by AF4-MALS-DLS

Figure 4.5a depicts the r_g (blue) and r_h (red) distribution plotted over the MALS 90° signal for the PEGylated particles, with the PSDs 20 – 35 nm and 34 – 43 nm respectively between retention times 12 – 16 min. In **Figure 4.5b**, an r_g/r_h ratio over MALS 90° graph is drawn to distinctly monitor the geometry of the particles, where for a uniform hard sphere, the quotient of the ratio is 0.775 (Gogos *et al.* 2014; Mukherjee and Hackley 2018). With a ratio distribution from 0.680 to 0.850, it is clear to highlight the suitable shape retention properties of the PEG on the spherical anatase particles. While the diameters of PEG are not precisely the same for each capped particle, this is dependent on the original shape of the uncapped TiO_2 NPs, as supported by the linear trends in distribution (**Figure 4.5a**).

With regards to the barycentre of the distributions i.e. the approximate peak maximum of the MALS 90° signal (at 14 min elution time), the calculated (n = 3) r_g, r_h and D_{geo} values for PEG-TiO_2 NPs corresponding to a sphere fit formalism were 28.7±1.1 nm, 40.3±2.0 nm and 74.0±2.4 nm, respectively. From the TEM analysis in **Figure 4.9a**, we observe the average size of d = 38.4 nm for the individual uncapped TiO_2 particles. With reference to the MALS data, we can simply deduce the size of the PEG corona to be D_{geo} = 35.6 nm (74.0 nm – 38.4 nm), revealing an almost identical size between the polymer and TiO_2 NPs. Ideally, a TEM micrograph would be assumed to reveal this information, but for the technique's inability to sufficiently observe polymer-based matrices due to difficulties in imaging caused by low contrast as a result of the relatively low mass elemental polymeric constituents (Patterson *et al.* 2012). However, it must be noted that the diameter of PEG coating for each TiO_2 particle may differ, as only an average measurement was stated above.

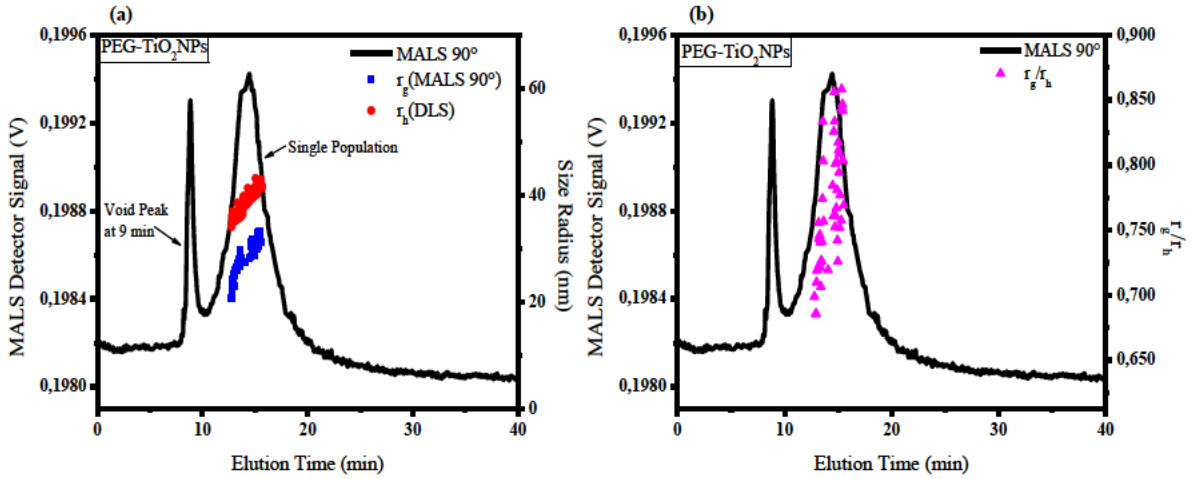

Figure 4.5. AF4-MALS-DLS fractograms of **(a)** r_g and r_h and **(b)** r_g/r_h over MALS 90° for 0.2 mg/ml PEG-TiO_2 NP suspension.

4.2.1.3) Size characterisation and distribution of TiO_2 NPs in commercial sunscreens by AF4-MALS-DLS

Here, we apply the above-developed method to commercial sunscreens. For the "nano" sunscreen (**Figures 4.6a-b**), we observed the PSDs for r_g, r_h and r_g/r_h as in the previous section, with the D_{geo} here determined to be 105.3 nm. However, establishing an estimation of the size relation between the particle and its coating in this matrix becomes challenging. While TEM does provide an idea of the TiO_2 core diameter (d = 42.4 nm), the particle corona is indistinguishable (**Figure 4.9b**). Returning to **Figure 4.6a**, we still observe linear trends for r_g and r_h, furthered by a minimal void peak and distinctly separated sample peak with no agglomerates visible. However, we notice an apparent partitioning between the upward trends of the r_g (blue) and r_h (red) plots. This can be explained by the DLS observing the possible presence of micelles arising from the sunscreen matrix interaction with the NovaChem carrier liquid. Crossing over to **Figure 4.6b**, the scant r_g/r_h values from 1.100 to 0.850 are representative of hollow sphere particles indicating a high diameter of coating in comparison to the core TiO_2 size (Lohrke, Briel and Mäder 2008). However, it is observed that most

particles detected are spherical or quasi-spherical in shape, as depicted by the dense population of particles with r_g/r_h ratios of 0.850 to 0.600, thus confirming the geometry of the particles present.

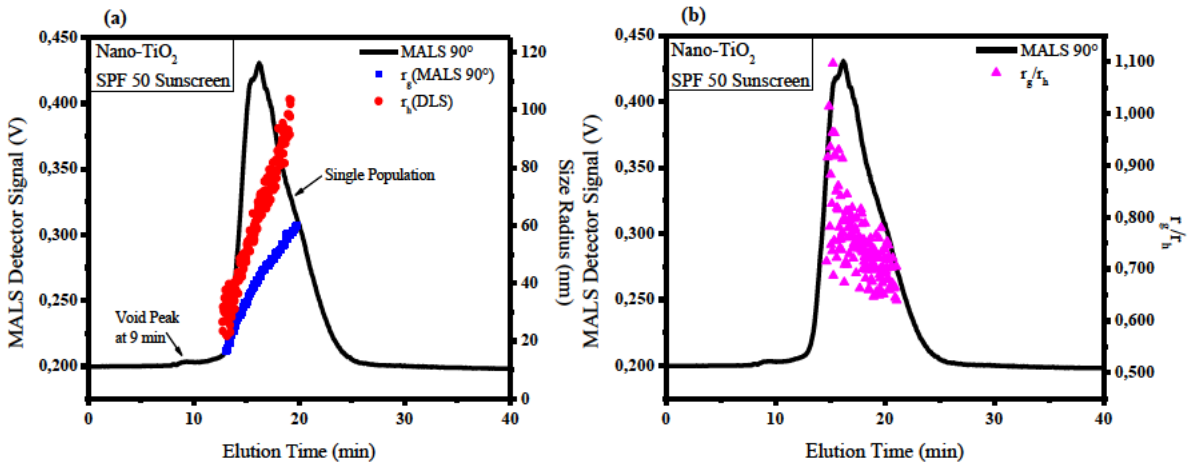

Figure 4.6. AF4-MALS-DLS fractograms of **(a)** r_g and r_h **(b)** r_g/r_h over MALS 90° for Nano-TiO_2 SPF 50 sunscreen.

Figures 4.7a-b highlight the more complicated challenges that analysts may come across whilst interpreting AF4-MALS-DLS data for commercial sunscreens. For the "unspecified" sunscreen, it must be reiterated that the labelling of the product in the ingredients list stated no indication of containing any nanoparticles, let alone that for TiO_2 (**Appendix 1**). Hence, it is interesting to report that the sample exhibited three distinct populations of particles (**Figure 4.7a**), with D_{geo} values of 58.1 nm, 61.7 nm and 318.9 nm respectively.

By inspection, we note the lack of separation between the minor void peak and "Population 1". This occurrence may appear non-ideal, however, it must be stated that this seems to be representative of clusters of relatively minute "spots" as per TEM analysis (**Figure 4.9c$_i$**), where the addition of grape, cranberry and Chinese fruit extracts as per the ingredients list may inadvertently account for the presence of naturally occurring NPs (Zhao *et al.* 2020). The sparsity of particles in this population, however, invariably decreases the likelihood of

obtaining a marginal error in size detection particularly due to the crossflow occurring optimally at a retention time reasonably distinct from that of the initial sample focusing step. However, this factor is entirely dependent on the nature and matrix of the sample being analysed. A view to modify the method slightly (possibly by changing the power decay of the crossflow for instance) to improve separation of the less distinct populations is open to the analyst; once again it is reiterated that this is sample dependent, looking in comparison to the single population determined in the "nano" sunscreen (**Figures 4.6a-b**). While the DLS exhibited noisy scattering as a possible consequence of the relatively small size of the particles, the MALS distribution was linear and steady, with an r_g PSD of 20 – 30 nm (**Figure 4.7a**), showing promise of stable analysis and separation at this size range. The r_g/r_h ratio data was not reliable for this population, due to the aforementioned scattering of the DLS detector.

"Population 2" denotes a strong signal intensity, representative of a high number of TiO_2 scattering centres. Interestingly, TEM analysis revealed the presence of rod-shaped rutile nanoparticles in the sample (**Figure 4.9c$_{ii}$**). The r_g and r_h values concur trend-wise, however, the superiority of the MALS detector is once more displayed relative to that of DLS, simply due to the variation of the radial distribution between the two detectors (r_g PSD = 15 – 45 nm; r_h PSD = 50 – 300 nm). Clearly, the complexity of this matrix, in particular, plays into the oversensitivity issues of the DLS technique (Malm and Corbett 2019). Consequently, much like "Population 1", not much could be exhibited from the r_g/r_h ratio curve.

Finally, with regards to "Population 3", we observe a low signal intensity (magnified in the insert) (**Figure 4.7a**). This is promising, as this minor peak indicates that most of the particles were dispersed in this analysis. We can concur that the agglomerated particles are irregular in shape, as indicated by the wide distribution of r_g/r_h values (0.250 to 2.000).

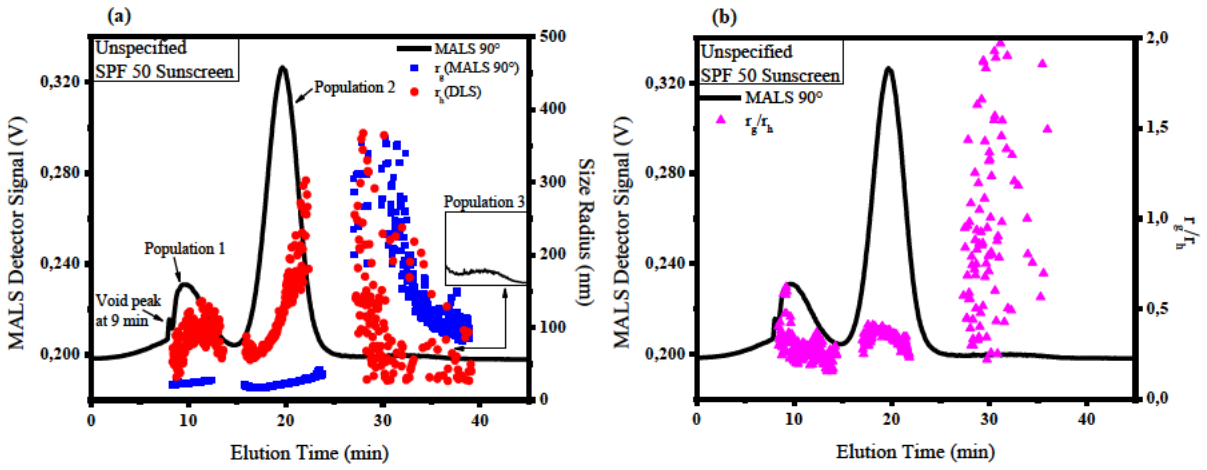

Figure 4.7. AF4-MALS-DLS fractograms of **(a)** r_g and r_h **(b)** r_g/r_h over MALS 90° for Unspecified SPF 50 sunscreen.

4.2.1.4) Size characterisation and distribution of TiO_2 NPs by spICP-MS

The spICP-MS particle size distribution of the uncapped TiO_2 NPs, PEG-TiO_2 NPs and sunscreen samples are shown in **Figures 4.8a-d**. In reference to the uncapped TiO_2 NPs (**Figure 4.8a**) the diameter (d) was observed at 50.0±3.0 nm due to possible agglomeration, whereas in the case of the PEG-TIO_2 NPs (**Figure 4.8b**), d = 32.0±3.0 nm; this shift in the size distribution is indicative of improved particle dispersion which is attributed to the strong binding interaction of PEG to individual TiO_2 NPs.

For the two sunscreen samples, the results suggest that both the "nano" and "unspecified" products contained TiO_2 NPs, with d = 42.0±4.0 nm and d = 49.0±5.0 nm respectively (**Figures 4.8c-d**). While the "nano" sunscreen sizing concurs closely with that of TEM (d = 42.4 nm), there is a discrepancy pertaining to the "unspecified" sample. The TEM diameter per individual TiO_2 rutile nanorod (**Figure 4.9c$_{ii}$**) averages to d = 103.1 nm, which is double that of the reported spICP-MS value. However, as per **Eq. (3.31)**, the instrument is calibrated for the detection of spherical particles. Further, particularly for **Figure 4.8d**, it must be noted that the Gaussian curve averages out all the data present in the given range, including those

observed from 100 - 250 nm which are possibly indicative of agglomerates. Additionally, the detection limit of $d > 15$ nm ultimately hides a portion of the first population detected close to the void peak by AF4-MALS-DLS for this sample (**Figures 4.7a-b**).

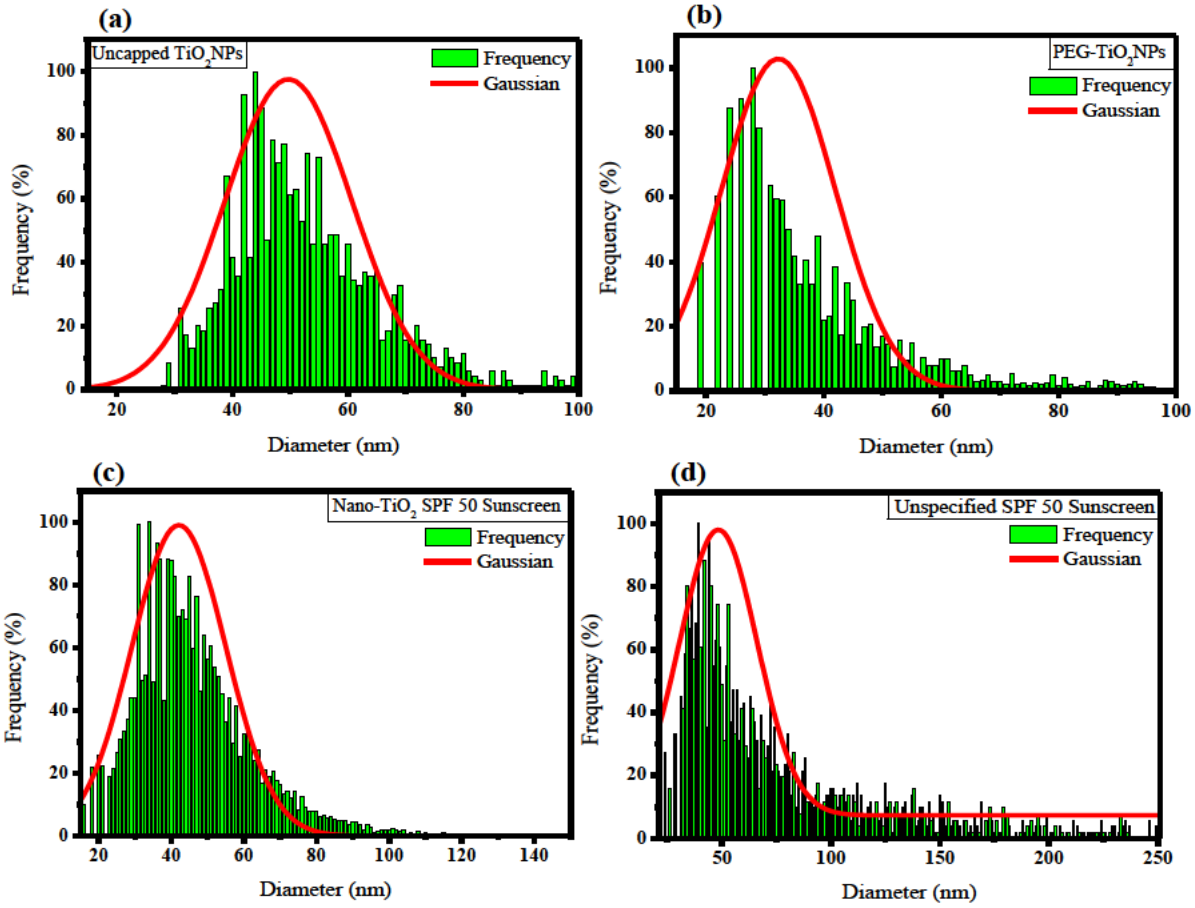

Figure 4.8. SpICP-MS particle size distributions for **(a)** Uncapped TiO_2 NPs **(b)** PEG-TiO_2 NPs **(c)** Nano-TiO_2 SPF 50 and **(d)** Unspecified SPF 50 sunscreen samples.

4.2.1.5) Size characterisation of TiO_2 NPs by TEM

TEM analysis was undertaken on the uncapped TiO_2 NP dispersion as well as the two sunscreen samples (after defatting by hexane) (**Figures 4.9a-c**). The results obtained for the uncapped TiO_2 NPs confirm the spherical shape with the size determined d = 38.4±3.8 nm (**Figure 4.9a**), with agglomeration visible as depicted by the dark spots circled in red. This may also explain the apparent slight variation in the size of individual nanoparticles, as smaller

particles are more prone to aggregation due to inter-particle van der Waals interactions. The marginally larger nanoparticles, on the other hand, tend to hold a comparatively higher potential energy barrier against the kinetically charged coalescing particles (Zhou *et al.* 2013). This behaviour tends to correspond with the uncapped TiO_2 NPs AF4-MALS-DLS analysis in **Figure 4.3**. Essentially, it must be expressed that the agglomerates in the fractogram referenced constitute of a large number of smaller particles, and not vice versa.

As per **Figure 4.9b**, it was observed that the "nano" sunscreen was found to have TiO_2 particles of d = 42.4±3.9 nm. Following the defatting by hexane procedure, any polymeric, silicone or alumina coating making up the sunscreen matrix would remain to take the shape of the particles, the purpose of which to counteract the photoactivity of the TiO_2 NPs (Skočaj *et al.* 2011). As noted earlier, these coronae were not able to be observed through TEM.

The same inhibitions apply to the "unspecified" sunscreen (**Figure 4.9c**) despite the differing ingredients. Interestingly, the sample denoted clusters of dark-spotted particles (d = 57.0±5.7 nm), possibly from the aforementioned plant extracts (**Figure 4.9c$_i$**). Further, a TiO_2 rutile nano-rod cluster was observed in the sunscreen matrix, with individual particles sized at d = 103.1±9.8 nm (**Figure 4.9c$_{ii}$**).

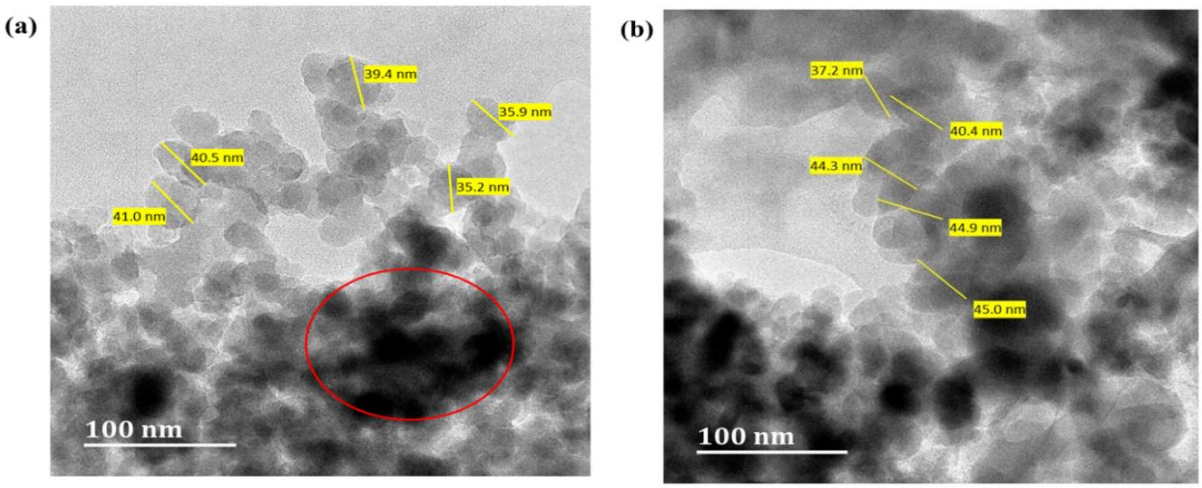

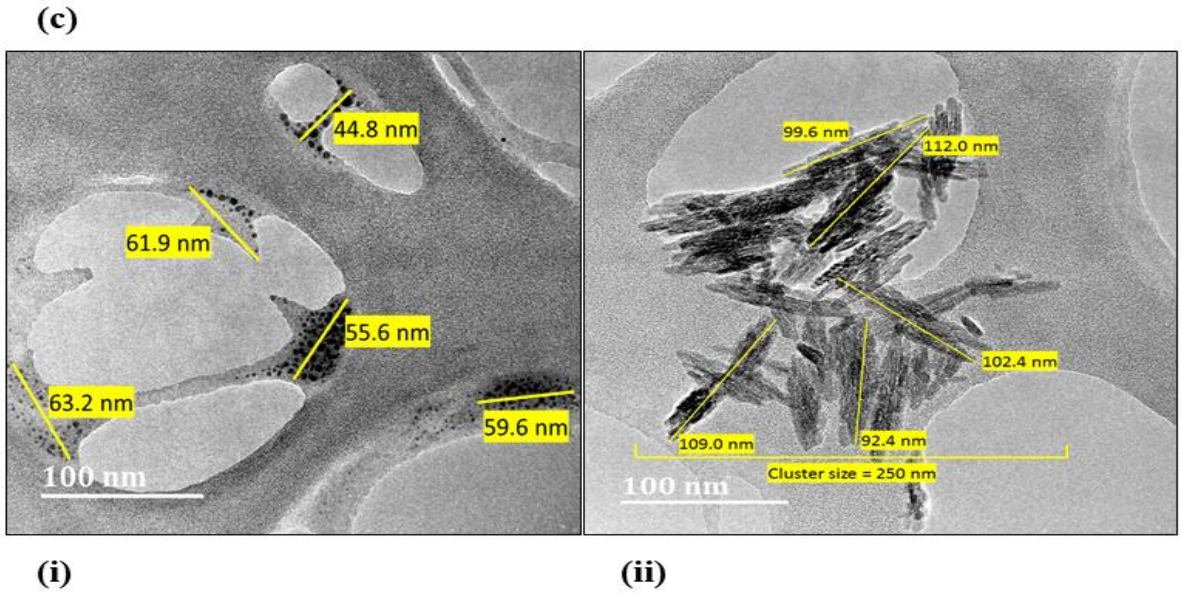

Figure 4.9. TEM images for **(a)** Uncapped TiO_2 NPs **(b)** Nano-TiO_2 and **(c)** Unspecified SPF 50 sunscreen samples.

4.2.1.6) Zeta potential, spectroscopic and thermogravimetric characterisation of TiO_2 NPs and PEG-TiO_2 NPs

Zeta potential studies were carried out to better understand the surface-particle interactions in aqueous medium. Firstly, the zeta potential of the uncapped TiO_2 NPs in solution was analysed (n = 3) to be 34.0±0.6 mV, as a result of the protonation of the O-H groups in solution at the relatively low pH of 5.6. A lowering of energy (13.8±0.8 mV) was observed in the case of the PEG-TiO_2 NPs. Further, both "nano" (-45.0±0.5 mV) and "unspecified" (-56.5±0.4 mV) sunscreens demonstrated even lower zeta potentials, indicative of increased surface energy stability. In short, a decrease in zeta potential increases the stability of a respective suspension due to enhanced electrostatic repulsion.

UV-Visible spectroscopy was used to characterize the photometric properties of the uncapped TiO_2 NPs, PEG, and PEG-TiO_2 NPs as illustrated in **Figure 4.10a**. The maximum absorption peaks for uncapped TiO_2 NPs and PEG were observed at 270 nm and 250 nm as reported by

López-Heras et al. (2014) and Zhu et al. (2019), respectively. In the case of the PEG-TiO_2 NPs however, a lower absorption was observed due to the strong binding interaction between PEG and TiO_2 NPs, resulting in the increased stability and lowering of the surface energy of the TiO_2 NPs. This is confirmed by the bathochromic shift for PEG-TiO_2 NPs.

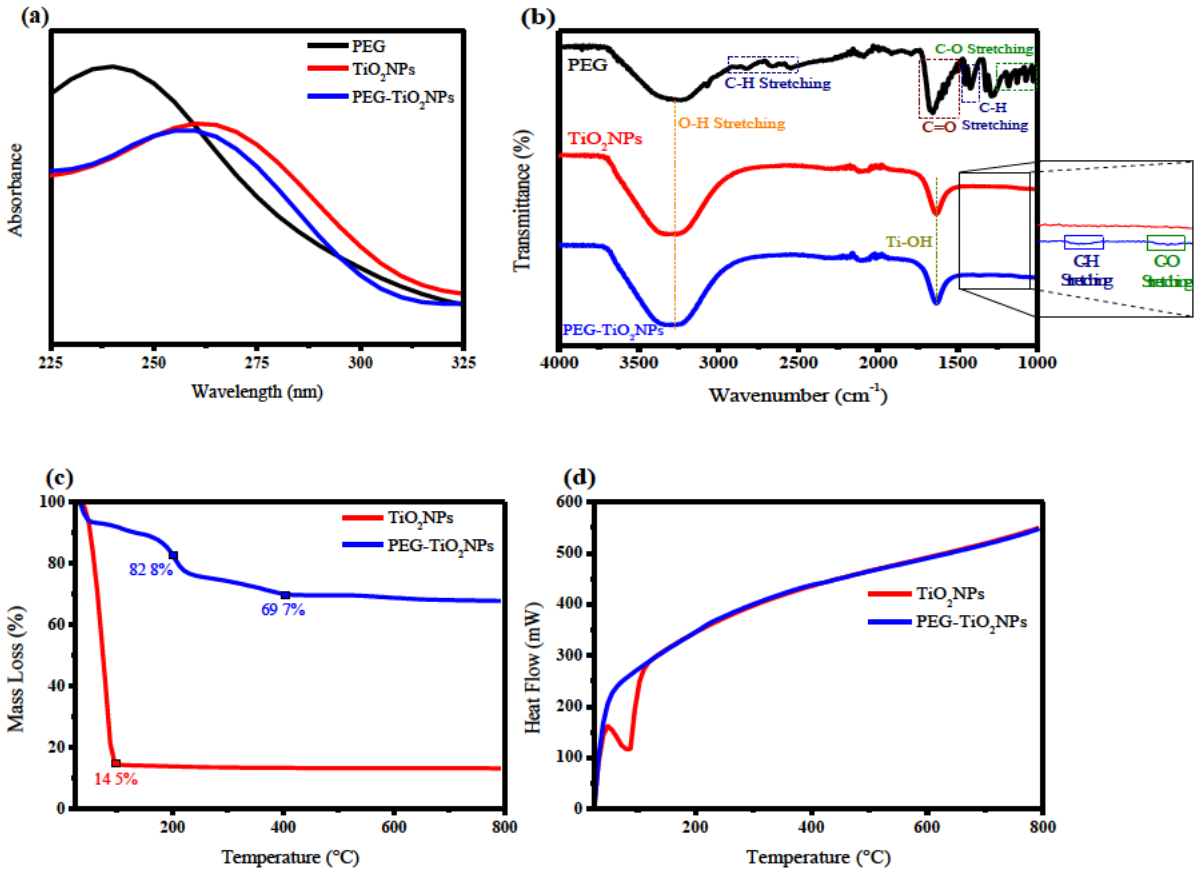

Figure 4.10. (a) UV spectrum **(b)** ATR-IR spectrum **(c)** TGA thermogram and **(d)** DSC thermogram of PEG, TiO_2 NPs and PEG-TiO_2 NPs.

The role of functional groups on PEG, TiO_2 NPs and PEG-TiO_2 NPs was investigated using ATR-IR from the wavelength range of 4000 cm^{-1} to 1000 cm^{-1}, as represented in **Figure 4.10b**. In the case of PEG, small broad peaks at 2856 cm^{-1} and 1364 cm^{-1} correspond to C-H stretching, whereas the small and sharp peaks from 1020 – 1275 cm^{-1} are attributed to C-O stretching. A sharp peak at 1656 cm^{-1} could be explained by the plausible formation of C=O, as one of the possibilities for PEG to undergo dissolution in an aqueous medium (Guilminot, Dalard and

Degrigny 2002). A large broad peak from around 3550 – 3200 cm^{-1} signifies O-H stretching from the PEG chain. In the case of TiO_2 NPs, the O-H band at 1630 cm^{-1} denotes the interaction of TiO_2 NPs with water molecules, resulting in the formation of Ti-OH (León *et al.* 2017). The ATR-IR spectrum of the PEG-TiO_2 NPs is very similar to that of the TiO_2 NPs, but for the prevalence of minor peaks from PEG at 1364 cm^{-1} and 1216 cm^{-1} corresponding to C-H and C-O stretching respectively, as shown in the extract (**Figure 4.10b**).

The thermal stability of the TiO_2 NPs and PEG-TiO_2 NPs were analyzed by TGA/DSC (**Figures 4.10c-d**). In the case of TiO_2 NPs, a single significant mass loss stage occurred in the temperature range of 25℃ to 100℃, as a result of rapid water loss from the aqueous matrix of the nanodispersion. Thereafter, the mass of the particles remained constant (at 14.5%) indicating the high-temperature stability of the TiO_2 NPs.

For PEG-TiO_2 NPs on the other hand, two mass loss steps were observed between temperatures 200 ℃ and 450 ℃. The first drop-down at 82.8% mass is possibly due to the formation of PEG peroxide at 200 ℃ in air (Han, Kim and Kwon 1997). The second drop-down (at 69.7% mass) is due to the degradation of the PEG polymer chain. Similar results were obtained by Voorhees et al. (1994) on a mechanism proposed for the hydrogen abstraction reactions and disproportionation of PEG. The PEG backbone possibly underwent a series of homolytic cleavages between the bonds of C-O and C-C, resulting in the polymer's degradation at higher temperatures.

4.2.1.7) Summative particle size evaluation

To evaluate the integrated role that each sizing technique plays in accordance with the samples analysed, a comprehensive, summarizing comparison of their findings in this study is required. In reference to **Table 4.1**, each detector, while different in principle, provides complementary

information pertaining to particle size characterization and distribution. On the other hand, it is not expected to achieve the same measurements for each technique. To interrogate, we first consider the uncapped TiO_2 NPs. As stated earlier, agglomeration and non-ideal scattering inhibited analysis by AF4-MALS-DLS. The latter interference was not a problem for spICP-MS and TEM however, as both detectors measure the "core" TiO_2 particle with the outer polymeric coating undetected. As such, the theoretical diameters "*d*" evaluated by the two techniques are directly comparable (Goenaga-Infante and Bartczak 2020). We did find, however, that after coating the uncapped TiO_2 NPs with the PEG, spICP-MS revealed a decreased size reading of the PEGylated particles, agreeing with the TEM measurements of the uncapped TiO_2, thus highlighting the polymer's dispersive capabilities. AF4-MALS-DLS analysis exhibited stable linear PSDs for both MALS and DLS detectors.

Considering the "nano" sunscreen, there was a close resemblance between the spICP-MS and TEM results, showing promise with regards to the efficacy of these techniques for mono-modal (specifically anatase-containing) TiO_2 sunscreen formulae. It looks to appear that the hexane defatting sample preparation step is capable of removing significant interferents from the original complex matrix of the sample. These findings concurred once again with the detection stability of the AF4-MALS-DLS analysis.

On the other hand, the analysis of the "unspecified" sunscreen analysis was found to be more challenging. This may stem from the sample containing TiO_2 rutile nanoparticles of a rod-like geometry. While TEM analysis directly confirmed the presence of these particles, this proved problematic for MALS, DLS and spICP-MS detection as despite the differing measurands, all the mentioned techniques are calibrated by means of spherical geometry modelling i.e. they assume the particles analysed as spheres. This may have resulted in understated size

measurements by MALS and spICP-MS, while the DLS analysis was hampered by non-ideal scattering.

Table 4.1. Summary of particle sizes evaluated from AF4-MALS, AF4-DLS, spICP-MS and TEM techniques (n = 3; associated ± error = STD Dev).

Sample	AF4-MALS (D_{geo}) - nm	AF4-DLS (D_h) - nm	spICP-MS (d) - nm	TEM (d) - nm
TiO_2 NPs	-	-	50.0±3.0	38.4±3.8
PEG – TiO_2 NPs	74.0±2.4	80.5±4.0	32.0±3.0	-
Sunscreen (Nano)	105.3±6.2	122.2.±8.3	42.0±4.0	42.4±3.9
Sunscreen (Unspecified)*	61.7±5.8	222.0±7.2	49.0±5.0	103.1±9.8

***Modal population with exception of spICP-MS.

4.2.2) Computational

Table 4.2 depicts trends in adsorption energies for the PEG/water adsorbate system with increasing TiO_2 particle size measurements. The table lists the adsorption energies based on the interactions between individual 2 nm, 4 nm and 6 nm uncapped TiO_2 anatase nanoclusters and 50 units of water, followed by an equivalent number of PEG units and lastly a combined 50:50 split ratio of the two compounds. For all sizes of the TiO_2 NPs with the reaction with water, similar E_{ads} (adsorption energy) are obtained with values of $E_{ads[2\ nm]}$ = -47.831 kcal/mol, $E_{ads[4\ nm]}$ = -46.168 kcal/mol and $E_{ads[6\ nm]}$ = -44.557 kcal/mol as per the simulation. Upon interaction with PEG, the adsorption energies lowered significantly in comparison to that of the water ($E_{ads[2\ nm]}$ = -471.924 kcal/mol; $E_{ads[4\ nm]}$ = -469.175 kcal/mol; $E_{ads[6\ nm]}$ = -401.826 kcal/mol), indicative of high adsorption and increased energy stability between the substrate and adsorbate. The adsorption energies are all negative, indicating that the adsorption process is exothermic and spontaneous. Clearly, there is a marked decrease in the adsorption energy for the addition of PEG compared to the addition of water onto the TiO_2 surface, suggesting that

TiO_2 strongly interacts with PEG. The computational modelling results demonstrated the strong binding affinity of PEG as a capping agent to TiO_2, exhibiting stabilisation of TiO_2 NPs in aqueous medium. This result demonstrates the effectiveness of PEG capped TiO_2 NPs to overcome agglomeration. However, minimal increases in adsorption energies with corresponding increases in TiO_2 particle size, suggest that the adsorbates can easily bind to the spherical nanoparticles, as illustrated in **Figure 4.11**.

Table 4.2. Adsorption energy interactions of adsorbates to TiO_2 NPs.

		No. of adsorbates molecules onto TiO_2 nanocluster		
Diameter of TiO_2 NP	**Adsorption Energy (E_{ads}) - kcal/mol**	**Water 50**	**PEG 50**	**Water: PEG 50:50**
2 nm	**E_{ads}**	-47.831	-471.924	-548.337
4 nm	**E_{ads}**	-46.168	-469.175	-463.141
6 nm	**E_{ads}**	-44.557	-401.826	-450.035

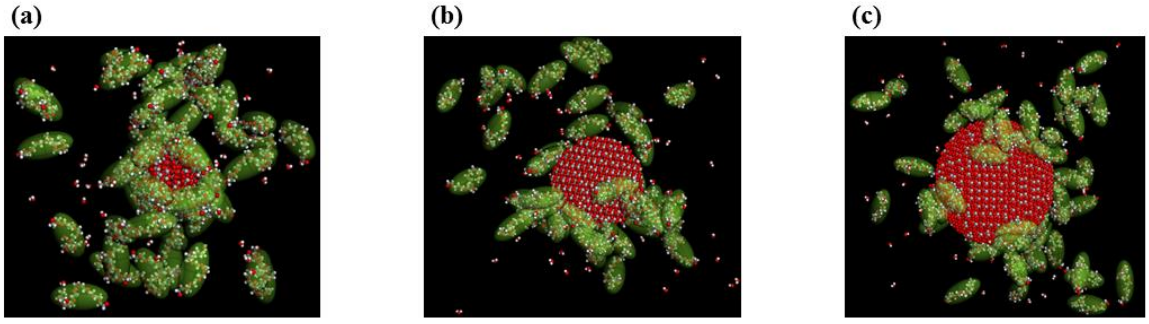

Figure 4.11. Optimized structures showing adsorption of 50 PEG: 50 water units to TiO_2 particles of sizes **(a)** 2 nm **(b)** 4 nm and **(c)** 6 nm. (The 3D structures for this study were generated using MS).

4.3) Summary

The encapsulation of TiO_2 NPs by PEG exhibited efficient particle dispersive and stabilization capabilities in AF4-MALS-DLS and spICP-MS analyses. These findings were furthered by the computational modelling study which deduced high adsorption affinities in the polymeric nanoparticle system. The commercial sunscreen analysis revealed MALS and DLS stability

towards the “nano” sunscreen, with r_g/r_h values of 0.600 to 0.850 confirming spherical geometry. Furthermore, TEM and spICP-MS achieved comparable sizing measurements of d = 42.4 nm and d = 42.0 nm, respectively. On the other hand, the “unspecified” sunscreen exhibited sizing challenges possibly due to the presence of rutile rod-like particles, as while these were detected, no clear correlation could be achieved between the aforementioned techniques without thorough interrogation. MALS, DLS, TEM and spICP-MS analyses did all, however, confirm the presence of nanoparticles in the sample, which completely contradicts the labelling of the product constituents as opposed to that of the “nano” sunscreen.

In the next case study, SiO_2 NPs in food samples are investigated also by experimental and computational methods. The adaptability of the AF4-MALS-DLS technique for nanoparticulate metal oxide analysis in complex matrices is further examined and supported by Monte Carlo adsorption simulations with supplementary interaction energy calculations.

CHAPTER 5

Case Study II – Multivariate optimization of Field-Flow Fractionation of nanoscale synthetic amorphous silica in processed foods supported by computational modelling

In this work, a multivariate approach has been developed to separate and characterise commercially available synthetic amorphous silica nanoparticles (SiO_2 NPs) potentially found in food products containing the additive E551. AF4-MALS-DLS in Flow mode was selected based on its potential to separate and determine the particle size and distribution within the nano-range (1-100 nm) of SiO_2 NPs in complex food matrices. Optimization by RSM of the experimental method involved the Box-Behnken design, incorporating the effects of crossflow, injection time and sonication time to enhance the baseline separation of the SiO_2 NPs. Accordingly, the performance of the developed method was evaluated using three commercial coffee creamer samples of different brands for SiO_2 NP analysis. UV-Vis Spectroscopy and Attenuated Total Reflectance Infrared (ATR-IR) Spectroscopy analyses were performed to assess the properties of the SiO_2 NPs by means of physicochemical characterization.
Moreover, an assessment of the adsorption phenomena of the silica nanoparticulate surface based on Monte Carlo simulations provides a better understanding of important surface phenomena, something that cannot be easily inferred from the experimentation alone. For this purpose, Monte Carlo simulations were employed in this study to assess the adsorption interactions between SiO_2 NPs and glucose in an aqueous environment.

5.1) Experimental

5.1.1) Chemicals and reagents

All chemicals used in this study were analytical grade. Ultrapure water (18.2 MΩ cm^{-1} resistivity at ambient temperature) was prepared by a Milli-Q Advantage A10 Water Purification System (Millipore, Amsterdam, Netherlands). NovaChem Surfactant 100 solution was purchased from Postnova Analytics (Landsberg, Germany). Sodium tetraborate (99.0%) and boric acid (99.99%) were purchased from Sigma-Aldrich (Johannesburg, South Africa). Silicon dioxide amorphous nanopowder (< 100 nm) was obtained from Sisco Research Laboratories (Mumbai, India).

Three commercial coffee creamers of different brands purchased from local retailers were selected with E551 on their ingredients' lists, each labelled sample A, B and C respectively (**Appendix 2**).

5.1.2) Sample preparation of commercial coffee creamers for AF4-MALS-DLS

Into a 50 ml plastic tube, 10 ml of hexane was added to a weighed aliquot of 0.1 g coffee creamer. The mixture was shaken thoroughly, sonicated for 30 min and then allowed to settle for 1 h. After 5 min of centrifugation at 3000 rpm, the clear hexane supernatant was carefully removed by pipette. Following the addition of 20 ml of 8 mM borax buffer solution to the remaining residue, the tube was vigorously shaken and finally sonicated for 30 min before analysis.

5.1.3) Instrumentation

5.1.3.1) AF4-MALS

The AF4 system (model AF2000 Multiflow, Postnova Analytics) was used in this study. The MALS detector (model PN3621, Postnova Analytics) was operated at 21 different angles, with 90° preferred as optimum. The AF4 channel flow rate was kept constant at 0.5 ml/min, with the pressure not exceeding 9 bars. A 350 μm spacer was used alongside a 10 kDa molecular weight cut-off regenerated cellulose membrane as the accumulation wall. The carrier liquid used was 8 mM borax buffer solution, which was prepared by dissolving 0.77 g sodium tetraborate and 0.25 g boric acid in 1000 ml ultrapure water. A 0.01 mg/ml amorphous SiO_2 NP suspension prepared in the above buffer was used to optimize the AF4 method, with the injection volume selected to be 80 μl. After optimisation, the selected parameters were crossflow at 0.8 ml/min

(with a stepwise exponential decay of 0.15, 0.70 and 0.90), injection time at 5 min and sonication time at 60 min.

5.1.3.2) AF4-DLS

The DLS measurements were performed in Flow mode after coupling to the AF4 by quartz flow cell using the Zetasizer (Nano ZS, Malvern Instruments Ltd., UK) and its software. Measurements were performed at 25℃.

5.1.4) Spectroscopic studies

In the wavelength range of 200 – 400 nm, the Varian Cary 50 UV-Vis Spectrophotometer analysed the SiO_2 amorphous nanoparticles in aqueous dispersion, while the ATR spectra were recorded from 4000 cm^{-1} to 1000 cm^{-1} on the Cary 630 FTIR Spectrometer (Agilent Technologies, Santa Clara, USA).

5.1.5) Experimental design

A Box-Behnken design with fifteen runs, three independent variables (crossflow, injection time and sonication time) and three centre points was used in this study. To protect the experiment against the effects of confounding variables, the data of the three factors were randomised prior to the generation of the factorial design. **Table 5.1** shows the experimental design of the three factors: crossflow, injection time and sonication time. The geometric diameter (D_{geo}) of the MALS detector after sphere fit formalism of each amorphous SiO_2 NP suspension run was taken as the response variable of the experiment, with analyses done in triplicate and an average for each reading obtained.

The statistical evaluation and correlation studies of the response of the model were undertaken with the use of Pareto charts, analysis of variance (ANOVA), interaction plots and estimated

response surface plots. The crossflow was varied from 0.8 to 2.4 ml/min, while the injection and sonication times were ranged from 3 to 7 min and 10 to 60 min respectively.

Table 5.1. Box-Behnken experimental design of 15 runs and 3 parameters for AF4-MALS amorphous SiO_2 NP response. The discrete values are listed in **Appendix 3**.

Run no.	Crossflow (ml/min)	Injection Time (min)	Sonication Time (min)	*Geometric diameter (nm)
1	1.6	7	10	32.54
2	0.8	5	60	30.69
3	2.4	5	60	29.96
4	1.6	7	60	30.60
5	0.8	3	35	30.26
6	1.6	5	35	35.03
7	1.6	3	10	29.71
8	1.6	5	35	32.54
9	1.6	5	35	38.29
10	0.8	7	35	31.57
11	2.4	5	10	37.17
12	0.8	5	10	31.94
13	2.4	3	35	32.09
14	2.4	7	35	34.09
15	1.6	3	60	31.86

*The average geometric diameter for three replicates.

5.1.6) Data analysis

STATGRAPHICS *Plus* version 5.1 was used for the preparation of the experimental design and data evaluation. NovaFFF AF2000 Software version 2.1.0.4® was used for peak integration and evaluation.

5.1.7) Computational modelling methodology

The construction of nanostructures is presented followed by structural examination using molecular mechanics (MM)-based geometry optimization. This is followed by interaction

studies using the Monte Carlo (MC) method towards predicting the adsorption process by means of the simulated annealing technique.

5.1.7.1) Construction of nanostructures and Forcite-geometry-based structural analysis

In this study, the substrate (SiO_2) and adsorbates (water and glucose) were constructed from the standard library of parameters of the Material Studio (MS) software package developed by BIOVIA (Ulicny and Kozar 2018).

For observing the feasibility of the structures, an energy minimization for each was performed followed by a geometry optimization using the Forcite module with the ultrafine-COMPASS force field (Sun 1998a). The convergence criteria for the maximum values of energy alteration, force, stress, and displacement were set at 2×10^{-5} kcal/mol, 0.001 kcal/mol/Å, 0.001 GPa, and 1×10^{-5} Å respectively.

In the case of the optimised unit cell of the SiO_2 nanostructures, a periodic supercell (3x3x1) with a vacuum slab thickness of 15 Å was constructed for adsorption studies with glucose and water.

5.1.7.2) Monte Carlo adsorption studies

Monte Carlo (MC) adsorption studies were applied to search for the lowest energy configurations of adsorbate on the surface of selected substrates as the temperature is gradually decreased. The Adsorption Locator (AL) module as implemented in the MS software was used as a preparatory and screening tool with the force-field method to obtain a ranking of the energies for each generated configuration, thereby indicating the preferred adsorption sites. Possible adsorption configurations are identified by carrying out Monte Carlo searches of the configurational space of the substrate-adsorbate system as the temperature is slowly decreased according to a simulated annealing protocol. The Ewald and group summation method in the

AL computes the non-bonding electrostatic and van der Waals interactions using different methods to improve the overall computational efficiency. The electrostatic interaction between glucose and SiO_2 is evaluated using charge groups. A charge group is a small group of atoms that are close to one another and which have a net charge of zero or almost zero. An electrostatic energy calculation is performed for each pair of charge groups whose centres are within the cut-off distance specified when the calculation is set up. Since charge groups are charge-neutral, the main error introduced by using a cut-off distance is due to dipole-dipole interactions. However, such interactions are usually low energy and act over short distances. Charge groups are defined automatically by default, but can also be set manually (Ulicny and Kozar 2018).

The generated adsorbate-substrate conformations for SiO_2-water, SiO_2-glucose and SiO_2-water/glucose were rank-ordered and the lowest adsorption energy conformers were each optimized using the Forcite-geometry optimization in order to reach a stable conformation.

5.2) Results and discussion

5.2.1) Experimental

5.2.1.1) BBD: Analysis of variance on analyte response

The Pareto chart displayed (**Figure 5.1**) is a graphical representation of individual and inter-factor interactions with the average geometric diameters D_{geo}, as determined in **Table 5.1,** indicated as the response variable. The magenta colour of a bar represents an effect that increases D_{geo}, while the red indicates a decreasing effect. Each bar proportionally expresses the standardised effect of the corresponding labelled factor, representative of individual t-statistics at 95% confidence level. Consequently, the blue line represents the t_{crit} value of 2.57 for 5 degrees of freedom at which for this experiment no effect extends beyond. While it

indicates that for this work no effects are statistically significant, it must be noted how influential the effect of ultrasonication (C) is on the separation of the amorphous SiO_2 NPs in the borax aqueous matrix, which Petersen (2014) defines as the use of high-frequency sound energy to break up particle agglomerates by cavitation, the implosion and expansion of bubbles. Its combination with the effect of crossflow is, however, the greatest relative effect (AC), a parameter that directly assorts particles by molecular weight resulting in elution of smaller sized SiO_2 NPs followed by the larger sized NPs. The effects of the other factors listed are comparatively negligible.

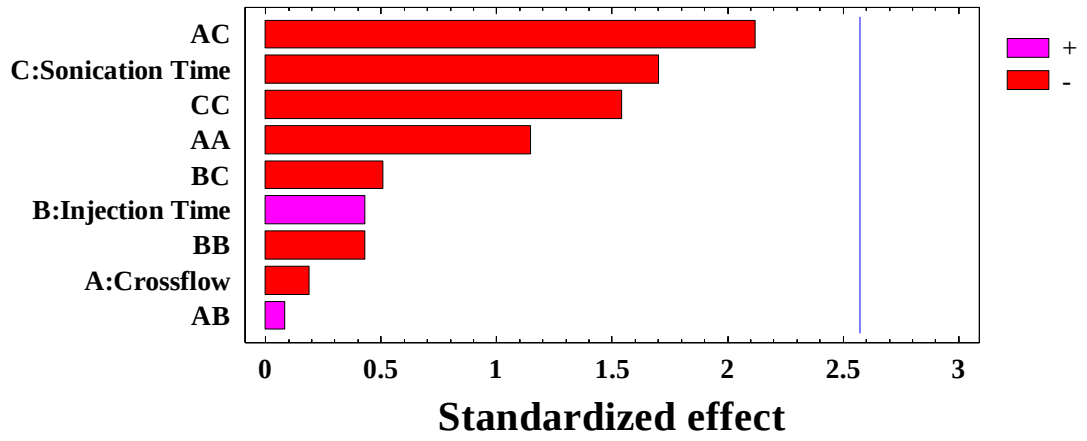

Figure 5.1. Standardized Pareto chart for D_{geo} (MALS) response.

The ANOVA table (**Table 5.2**) represents a summative set of results which statistically compares the variances of each independent factor separately (A, B and C) in relation to a corresponding response variable (D_{geo}). The mean square per factor level, as obtained from the quotient of the sum of squares and degrees of freedom, is compared to the mean square due to an estimate of the experimental error per individual data response, from which subsequent related F-ratios and P-values for each factor is generated. At 95% confidence level, none of the effects is significantly different from zero, as for all cases the P-values are greater than 0.05. Further analysis revealed that the fitted model as per the R-squared statistic explains 69.47% of

the variability in D_{geo}. The correlation matrix as shown in **Table 5.3** expresses the extent of the confounding or lurking variables amongst the effects. All non-zero terms off the diagonal with 1's imply correlation corresponding to the column and row of the respective effects, of which for this experiment there are three pairs on the matrix. However, since the values are less than 0.5, the extent of those lurking variables amongst the factors are deemed negligible. The output of residual studies, which describe the degree of correlation of the data between those experimentally inputted from the factors against the given response, was calculated and represented by the Durbin-Watson (DW) statistic and associated P-value for the model. The close proximity to the value 2 for the DW test (DW = 1.724) and the related P-value being greater than 0.05 (P = 0.4032) ensures that there is no indication of serial autocorrelation in the residuals. Ultimately, the ANOVA entails that the effects with the most influence on D_{geo} are the sonication time (C) and crossflow by sonication time (AC), due to the values' tendency towards the P-value of 0.05 (P_C = 0.1493; P_{AC} = 0.0876); this trend corresponds with the Pareto chart analysis discussed above.

Table 5.2. ANOVA - Estimated effects based on total error and interactions.

Source	Sum of Squares	Degrees of Freedom	Mean Square	F-Ratio	P-Value
A: Crossflow	0.578581	1	0.578581	0.04	0.8567
B: Injection Time	2.98378	1	2.98378	0.19	0.6838
C: Sonication Time	46.396	1	46.396	2.90	0.1493
AB	0.117551	1	0.117551	0.01	0.9350
AC	71.8377	1	71.8377	4.49	0.0876
BC	4.17327	1	4.17327	0.26	0.6313

Table 5.3. Correlation matrix showing extent of confounding interactions amongst effects.

	1	2	3	4	5	6	7	8	9
A: Crossflow	1.00	0.00	0.00	0.00	0.00	0.00	0.00	0.00	0.00
B: Injection Time	0.00	1.00	0.00	0.00	0.00	0.00	0.00	0.00	0.00
C: Sonication Time	0.00	0.00	1.00	0.00	0.00	0.00	0.00	0.00	0.00
AA	0.00	0.00	0.00	1.00	0.00	0.00	-0.07	0.00	-0.07
AB	0.00	0.00	0.00	0.00	1.00	0.00	0.00	0.00	0.00
AC	0.00	0.00	0.00	0.00	0.00	1.00	0.00	0.00	0.00
BB	0.00	0.00	0.00	-0.07	0.00	0.00	1.00	0.00	-0.07
BC	0.00	0.00	0.00	0.00	0.00	0.00	0.00	1.00	0.00
CC	0.00	0.00	0.00	-0.07	0.00	0.00	-0.07	0.00	1.00

5.2.1.2) BBD: Interaction studies

The Box-Behnken model allows for the generation of cross factor surface and interaction plots in response to the average geometric diameters D_{geo} from **Table 5.1**, as shown in **Figures 5.2-5.4**. The relationship between all three factors in this study via pairs in relation to each other is illustrated in **Figure 5.2**. For each pair on the x-axis, the first letter or factor mentioned is plotted from its lowest to highest values against the second factor from which two responses are generated - one held at its lowest value (indicated by "-") and the other at its highest value ("+") - as a function of D_{geo} on the y-axis. All other factors besides the two involved in the interaction are held constant at their central values. With regards to the factors of crossflow and injection time (AB), it is noted that both the high and low values of the latter factor appear to have a similar response to D_{geo} however, only a negligible size deviation is inhibited against separation as indicated by the minute overall increase in response. The effect of crossflow with sonication time (AC) is considerably more significant, with the low and high levels of the latter factor causing an increase and decrease of D_{geo} = 8 nm and D_{geo} = 9 nm respectively. Thus, if the separation is held at maximum sonication time (60 min) more particles are disaggregated

corresponding to an increase in crossflow; a contrast is observed at minimum sonication time (10 min), indicating that crossflow could promote agglomeration of particles if they are not sonicated sufficiently, as the SiO_2 NPs are pressed against the accumulation wall of the separation channel. This results in particles ultimately coalescing and eluting out further aggregated. Lastly, for the injection time with sonication time effect (BC), a clear distinction is seen for the D_{geo} measurements held at the minimum and maximum durations of sonication with the latter factor achieving the lower response. The minimum factor limit can be explained by the increase in time of the suspension of insufficiently sonicated particles following injection against the counter stream of the focus flow thus resulting in possible aggregation occurring within the channel. The maximum factor limit underlines the proficiency of the focusing step as minimal re-agglomeration of sonicated particles occurs.

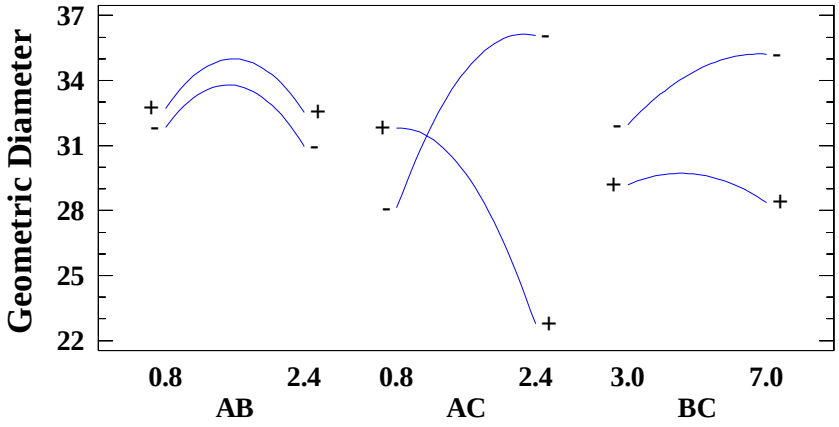

Figure 5.2. Interaction plot for D_{geo} (MALS) response.

The estimated response surface plots shown in **Figures 5.3 and 5.4** differ from the interaction plot (**Figure 5.2**) in that the factors held constant are at values selected experimentally (Crossflow = 0.8 ml/min; Sonication time = 60 min). It is found that D_{geo} measurements are consistent throughout the range of injection times if samples are sonicated for 60 min (**Figure 5.3**). Furthermore, a crossflow of 0.8 ml/min held at 60 min sonication time allows for

maximum particle separation at the lowest estimated D_{geo} response of 20.8 nm at an injection time interval between 3 and 6 min (injection time of 5 min selected experimentally) as shown in **Figure 5.4**. These observations highlight the separation efficiency of the optimised method for amorphous SiO_2 NPs.

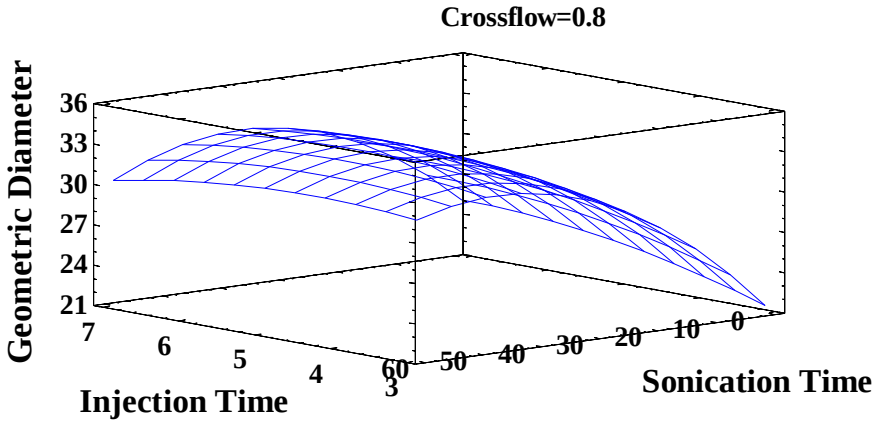

Figure 5.3. Estimated response surface plot for D_{geo} (MALS) response of injection time vs sonication time at constant crossflow of 0.8 ml/min.

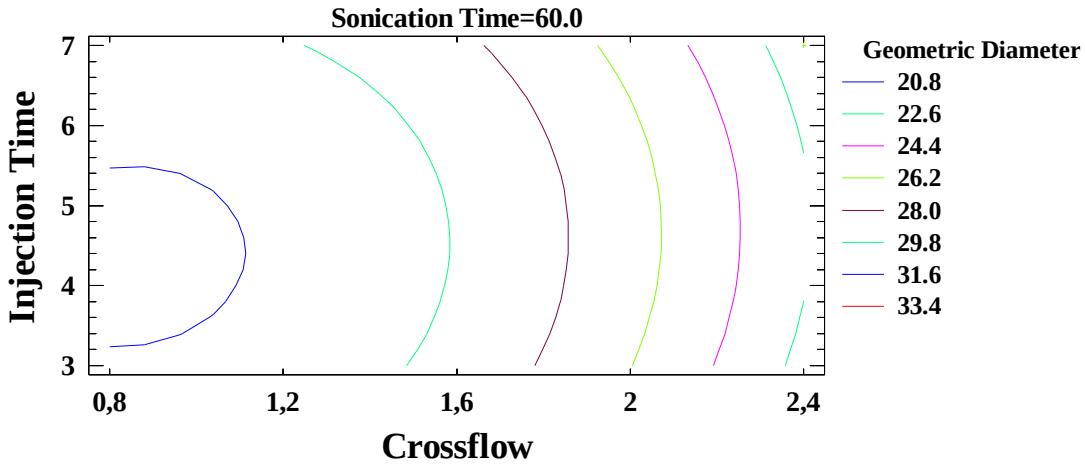

Figure 5.4. Contours of estimated response surface plot for D_{geo} (MALS) response of crossflow vs injection time at constant sonication time of 60 min.

5.2.1.3) Optimisation of AF4-MALS-DLS method

Table 5.1 shows the fifteen runs generated from the Box-Behnken model using crossflow, injection time and sonication time for the 0.01 mg/ml amorphous SiO_2 NP solution. The corresponding responses obtained for D_{geo} (MALS) follows the geometric spherical fit using the instrument software. **Figure 5.5** shows an overlay of the fractograms obtained for each run (n = 3).

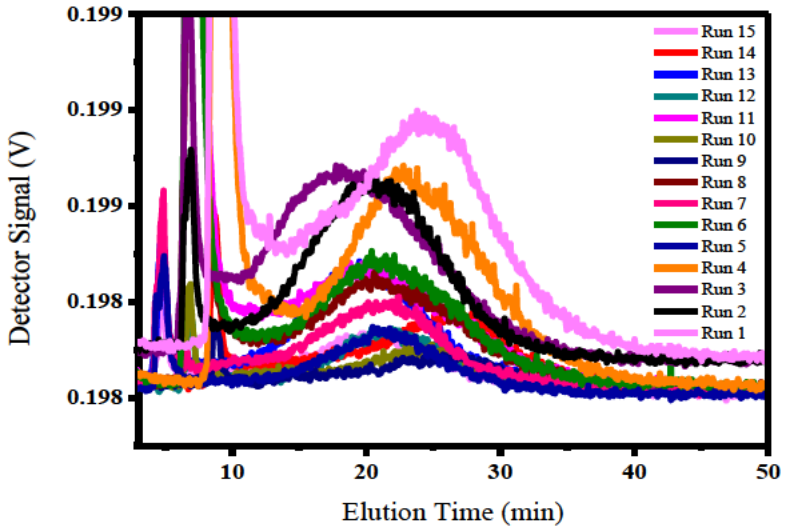

Figure 5.5. AF4-MALS fractogram overlay of amorphous SiO_2 NP fractograms from Box-Behnken experimental design at MALS 90°.

Run 2 was selected as the optimum plot displayed in **Figure 5.6**, based on the distinguishable baseline separation at an elution duration from 13-27 min achieved for the analyte peak compared to the shouldering and high void peaks obtained by the other runs. The characteristic amorphous SiO_2 NP void peak at these experimental parameters occurred at 7 min. Hence, the optimised parameters from the experimental design (as per **Run 2**) were determined as crossflow = 0.8 ml/min, injection time = 5 min and sonication time = 60 min. The r_g determined as per spherical formalism from AF4-MALS was 11.89 nm, with the resultant D_{geo} = 30.69 nm. The AF4-DLS result reported a measurement of D_h = 35.33 nm, which may have been impacted

by the excessive scattering as indicated by the detector's r_h distribution in **Figure 5.6**. Subsequently, an r_g/r_h value of 0.673 may appear understated as we expect a form factor closer to 0.775 for particles of spherical geometry (Lohrke, Briel and Mäder 2008).

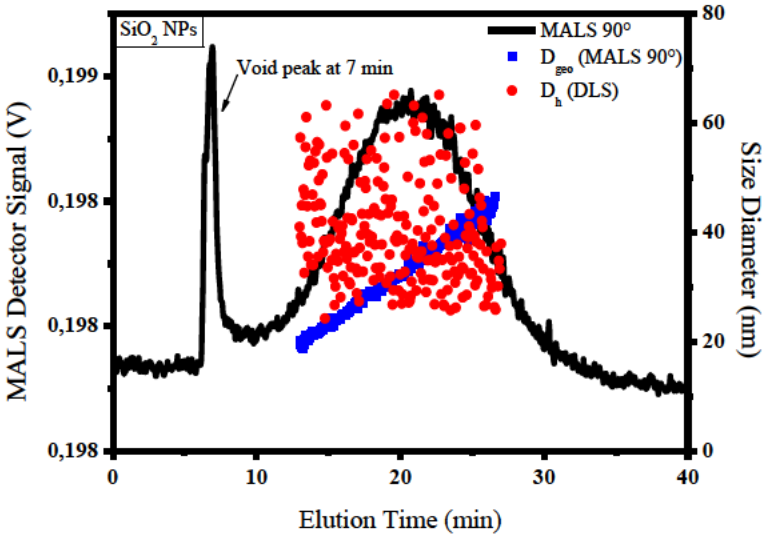

Figure 5.6. AF4-MALS-DLS fractogram of amorphous SiO_2 NPs; crossflow = 0.8 ml/min, injection time = 5 min and sonication time = 60 min (**Run 2**).

5.2.1.4) Size characterisation and distribution of SiO_2 NPs in commercial coffee creamers by AF4-MALS-DLS

The performance of the optimised method evaluated using three coffee creamer samples (E551) demonstrated size distributions for SiO_2 NPs ranging from 100-600 nm, 70-250 nm and 80-400 nm for samples A, B and C respectively as shown in **Figures 5.7a-c**.

A closer inspection of each sample reveals a relatively noisy scattering AF4-MALS signal intensity, as depicted in **Figure 5.7b**. This can be attributed to a relatively scant population of particles, as indicated by a comparatively lower signal intensity coinciding with a smaller particle size distribution. In **Figures 5.7a and 5.7c**, the SiO_2 NPs are dispersed much more evenly for AF4-MALS, with AF4-DLS indicating more scattering. This is expected due to the

complexity of the coffee creamer matrices. In summary, the calculated (n = 3) D_{geo} values determined from AF4-MALS for samples A, B and C were 286.7 nm, 129.8 nm and 190.7 nm respectively. This was followed by AF4-DLS D_h measurements of 301.5 nm, 141.3 nm and 197.8 nm respectively. As such, r_g/r_h values of 0.737, 0.712 and 0.747 were obtained, denoting spherical geometry for the particles in all three coffee creamers, as illustrated in **Table 5.4**.

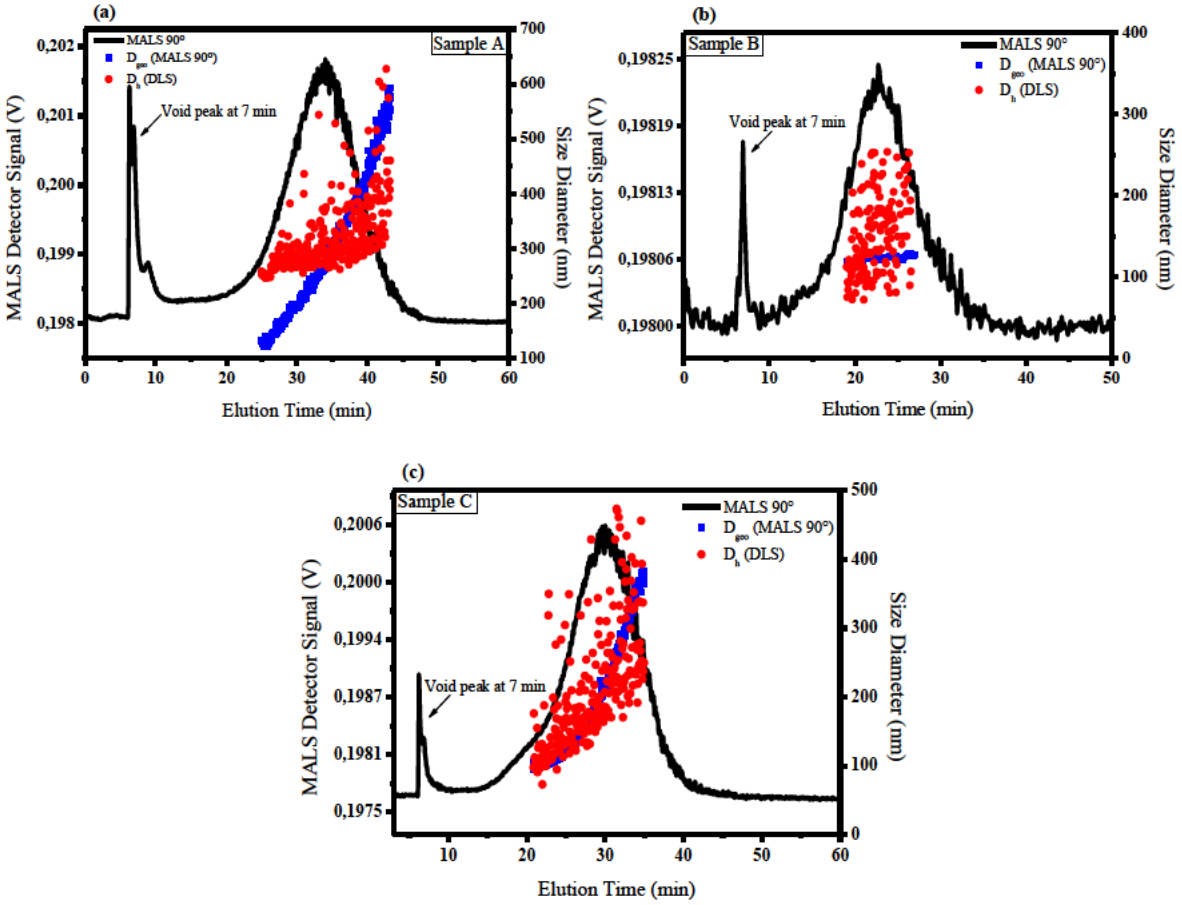

Figure 5.7. AF4-MALS-DLS fractograms of **(a)** Sample A and **(b)** Sample B and **(c)** Sample C coffee creamer samples.

Table 5.4. Summary of particle sizes from AF4-MALS and AF4-DLS techniques (n = 3; associated ± error = Standard Deviation).

Sample	AF4-MALS (r_g) - nm	AF4-MALS (D_{geo}) - nm	AF4-DLS (D_h) - nm	r_g/r_h
A	111.1±1.8	286.7±4.6	301.5±7.5	0.737
B	50.3±2.6	129.8±6.7	141.3±12.9	0.712
C	73.9±1.3	190.7±3.4	197.8±5.2	0.747

5.2.1.5) Spectroscopic characterization of amorphous SiO_2 NPs

The photometric and functional group properties of amorphous SiO_2 NPs were characterized by UV-Visible and ATR-IR Spectroscopy (**Figures 5.8a-b**). The maximum characteristic UV absorbance was observed at a wavelength of 270 nm. The ATR-IR spectrum revealed that at 3400 cm^{-1} the small band signifies O-H stretching due to the adsorption of moisture by the nanopowder. Additionally, the sharp peak at 1070 cm^{-1} is indicative of Si-O-Si asymmetric stretching while the smaller band at 910 cm^{-1} represents the Si-OH bond (Verma and Bhattacharya 2018).

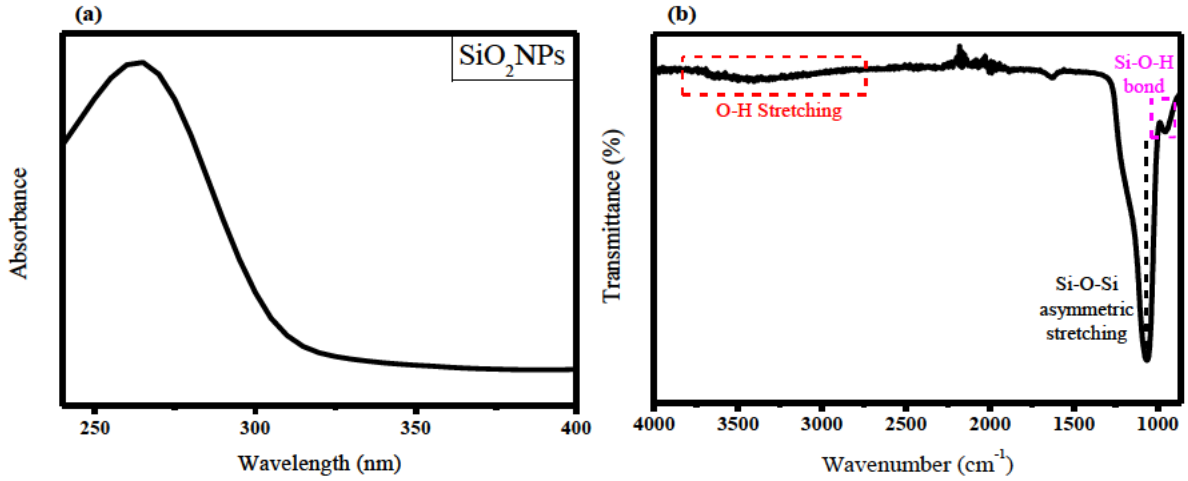

Figure 5.8. (a) UV spectrum **(b)** ATR-IR spectrum of amorphous SiO_2 NPs.

5.2.2) Computational

In this study, the Adsorption Locator (AL) was employed to simulate the SiO_2 substrate loaded with the adsorbates (glucose and water) individually and then as a mixture of a fixed composition of the adsorbates. Prior to performing the adsorption locator calculation, the substrate and adsorbates were constructed and optimized using the Forcite-geometry as described in the Methodology section. The approach used in this study to define the adsorption region of the substrate, was consequently required to specify a region around the target atoms. The simulated annealing task in the AL simulates a substrate loaded with an adsorbate or an adsorbate mixture of fixed composition. A low energy adsorption site is identified by carrying out a Monte Carlo (MC)-based function for the most favourable configurational space of the adsorbate (glucose and water) molecules towards the SiO_2 surface along a slowly decreasing temperature. During the course of the simulation, adsorbate molecules are randomly rotated and translated around the substrate. The resulting configuration is accepted or rejected according to the selection rules of the Metropolis Monte Carlo method (Metropolis *et al.* 1953).

Herein, to minimize computational costs, the adsorption behaviour of SiO_2 with varying 10 molecules of the glucose : water compositions were investigated.

The resulting low energy stable trajectories within the various mixtures along with the distribution fields are depicted in **Figure 5.9**. The configuration of the 10 water molecules tends to be in a planar position right above the Si target atoms, exhibiting a strong interaction (**Figure 5.9a)**. In contrast, upon replacing the water molecules with 10 glucose molecules, the distribution of the glucose adsorbate is adsorbed at the top of the vacuum region, instead of at the surface region (**Figure 5.9b**). Interestingly, the combination of equal amounts of

glucose/water adsorbates as depicted in **Figure 5.9c**, indicates glucose adsorption mainly at the top of the vacuum region, while the water molecules adsorbed closer to the SiO_2 surface.

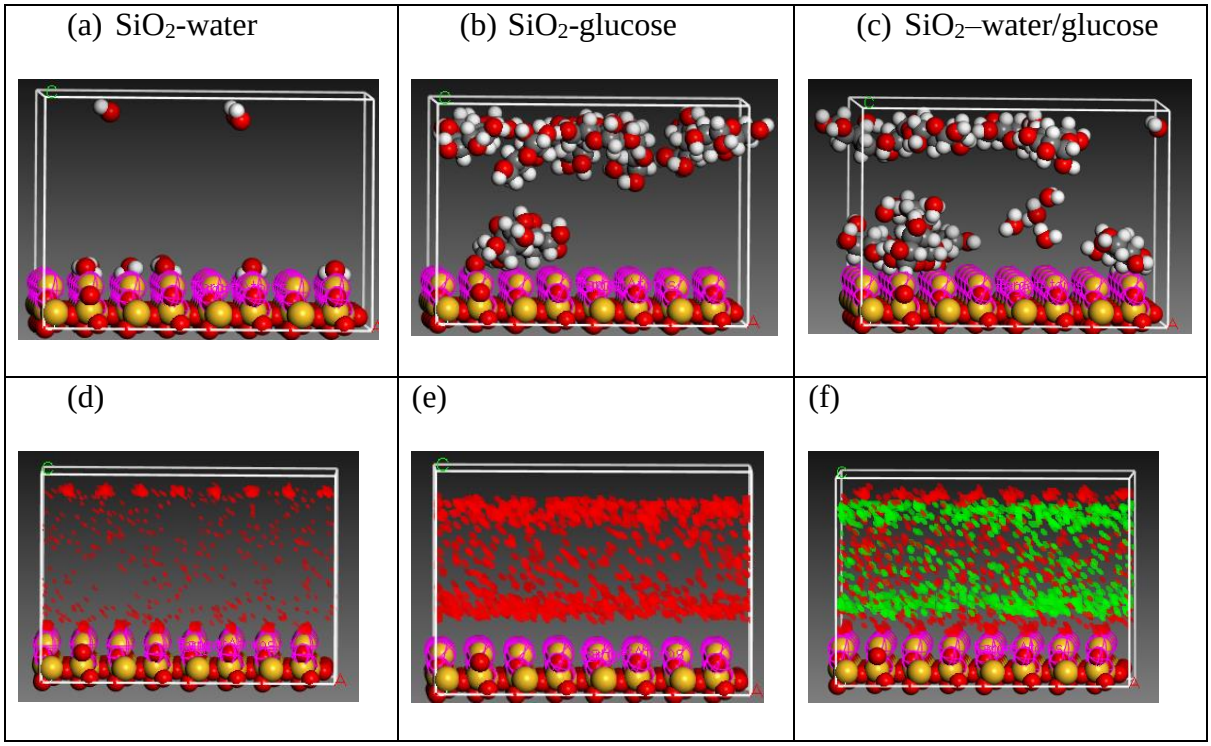

Figure 5.9. System conformations and distribution fields of ratios of SiO_2, water and glucose. The Si and O atoms are denoted in yellow and red respectively for SiO_2. With regards to water and glucose, the C, H and O atoms are depicted in grey, white and red, respectively. (The 3D structures for this study were generated using MS).

The evidence of these findings is confirmed by the favourable isosurfaces or heat field maps depicted in **Figures 5.9d-f**, with the more likely adsorption areas shown in green and the less likely sites appearing in red. Here, the "observed clouds" indicate the level of the distribution fields of the adsorbed molecule/s' location corresponding to the SiO_2 surface. The thickness of the distribution field corresponds to a higher accumulation of the adsorbate location. From this depiction, it is deduced that the water adsorbate molecules are adsorbed closer to the SiO_2 substrate surface than to the glucose adsorbate molecules. On the other hand, the vacant region in between remains an implausible area for glucose adsorption. The highest adsorption energy is generated by the SiO_2-water system, followed by the SiO_2-glucose system and thereafter the

SiO_2-water/glucose system. **Figure 5.10** shows the overall total energy, comprising of the average total energy, van der Waals energy, electrostatic energy and intramolecular energy calculated for the optimised SiO_2-water/glucose system.

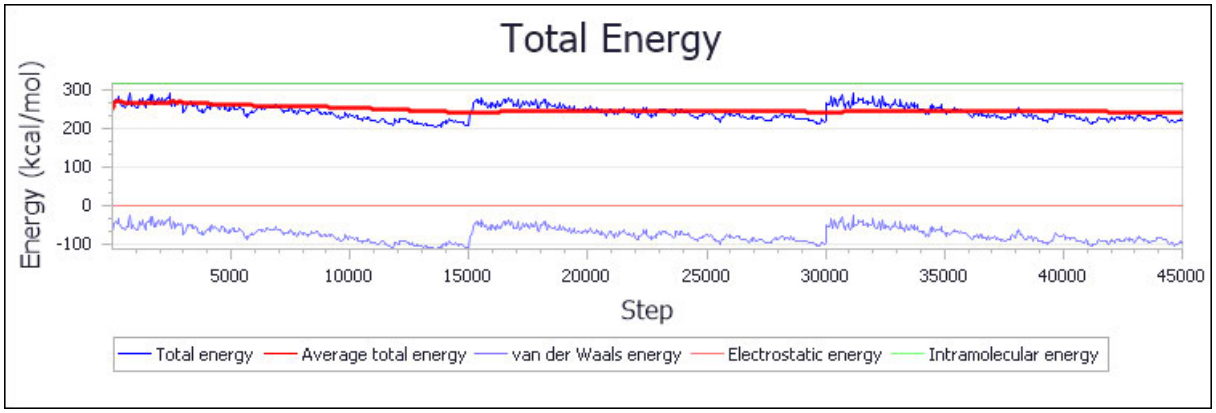

Figure 5.10. Overall total energy of SiO_2-water/glucose system.

This evidence is further elucidated by **Table 5.5,** which contains several energy contributions for the various loadings. This demonstrates that the inclusion of water molecules plays an essential role in directing the molecular adsorption of glucose and this is related to the variation of adsorption energies presented in the table below.

Table 5.5. Energy distribution (kcal/mol) of 10 adsorbates (water/glucose) onto the SiO_2 (substrate) surface.

Structures	**Total energy**	**Adsorption energy**	**Rigid adsorption energy**	**Deformation energy**	**Glucose : *dEad/dNi***	**Water : *dEad/dNi***
SiO_2 (substrate)	0	-	-	-	-	-
Water	0,00001	-	-	-	-	-
Glucose	31,5804	-	-	-	-	-
SiO_2-Water	-33,1598	-33,1604	-33,1665	0,0061	-	-2,4992
SiO_2-Glucose	103,8436	-211,9599	-122,7072	-89,2527	-19,6857	-
SiO_2-Glucose/Water	76,6992	-239,1049	-149,4619	-89,6430	-21,7571	-0,2336

The parameters presented in **Table 5.5** provide energetic details of the substrate-adsorbate configuration, as calculated during the run. In this study, the total energy of the SiO_2-water/glucose configuration is the sum of energies of the adsorbate components, the rigid adsorption energy, and the deformation energy, with that of the SiO_2 substrate being zero in this study. Additionally, the adsorption energies are all negative, indicating that the adsorption process is exothermic and spontaneous when the relaxed water/glucose (adsorbate) components are adsorbed on the SiO_2 (substrate). This is the sum of the rigid adsorption energy and the deformation energy for the water/glucose components. Clearly, there is a marked decrease in the adsorption energy for the addition of the water/glucose composition onto the SiO_2 surface, suggesting that SiO_2 strongly interacts with the water/glucose (adsorbate) mixture. The rigid adsorption energy refers to the energy released when the unrelaxed (water/glucose) adsorbate components, prior to geometry optimization, are adsorbed onto the SiO_2 substrate. This decrease in the rigid adsorption energy signifies a strong interaction of the unrelaxed water/glucose molecules onto the target atoms of SiO_2 surface. Interestingly, a similar energy value for the deformation energy suggests that there is little or no difference when the adsorbed water/glucose components are relaxed on the SiO_2 surface. **Table 5.5** also shows *dEad/dNi*, the energy in kcal/mol of the SiO_2-water/glucose configuration where one of the adsorbate components has been removed. The subsequent addition of glucose or water respectively, lowers the *dEad/dNi* energy value of the SiO_2-water/glucose configuration, with glucose having a significant impact in the adsorption process.

5.3) Summary

There is a growing need to disclose the possible presence of SiO_2 NPs on the labelling of commercial food products. Therefore, this work proposed an experimental design implementing the multivariate optimisation of AF4-MALS-DLS for the size characterization

of amorphous SiO_2 NPs. The findings reveal that AF4-MALS-DLS could be employed for the analysis of challenging media, particularly for samples with broad particle size distributions (PSDs). The technique was applied to three different commercial coffee creamers labelled A, B and C confirming the presence of SiO_2 NPs, with size distributions of PSD_A = 100-600 nm, PSD_B = 70-250 nm and PSD_C = 80-400 nm using AF4-MALS-DLS determined respectively. Spectroscopic analysis revealed the hygroscopic nature of the SiO_2 NPs in powdered form as indicated by the observed O-H stretching. Based on the computational results, we conclude that water plays an essential role in the binding of glucose to the SiO_2 substrate on the surface as an intermediate system stabilizing the adsorbate bridge. Finally, the outcomes of this study can also potentially be used to assess the particle size characterization of SiO_2 NPs in complex food matrices, contributing to future nano-labelling requirements.

CHAPTER 6 – CONCLUSIONS AND FUTURE PERSPECTIVES

6.1) Conclusions

Case Studies I and II involved the analysis of TiO_2 and SiO_2 NPs in cosmetics and food respectively. Methods for the size characterization and quantification of each analyte were developed for the AF4-MALS-DLS technique. Also, for both studies, computational methodologies were employed to interrogate the interactions of the respective nanoparticulate substrate-adsorbate systems.

In Case Study I, the sizing and separation of TiO_2 NPs in sunscreens were performed and correlated by AF4-MALS, AF4-DLS, spICP-MS and TEM. The physicochemical characterisation revealed the strong affinity of PEG to TiO_2 as a proficient polymeric capping agent due to decreased surface-particle energy readings as indicated by zeta potential and UV analyses. Thermogravimetric analyses confirmed the high thermal stability of the TiO_2 NPs. The aforementioned low interaction energy observations between PEG and TiO_2 nanoclusters were duly supported by the computational adsorption studies, thus confirming the stabilizing effect of the polymer.

Case Study II entailed the separation and size characterization of SiO_2 NPs in commercial coffee creamers by AF4-MALS-DLS. The multivariate optimization procedure involved the Box-Behnken design which implemented the randomized statistical generation of runs upon which the experiment was conducted; optimized conditions were established for the crossflow rate, injection time and sonication time. The binding mechanism of water in the SiO_2-glucose system was highlighted by both spectroscopic and MC adsorption analyses, thus depicting strong interactions between these substances when consumed in foods.

It must be reiterated that there are currently no regulations in place for the declaration of nano-enabled products by manufacturers in South Africa. This is in contrast to the nano-labelling requirements in force around the world, for instance in the European Union. These findings further exemplify the need for efficient nanomaterial regulation in South Africa.

6.2) Future perspectives

Future work can be directed towards and include an in-depth study pertaining to the adsorption affinity of SiO_2 and TiO_2 NPs to important biological and environmental matrix constituents dissolved in human albumin serum. Further, the study will involve the coupling of FFF techniques with ICP-MS for trace elemental analysis. This will be to understand the interaction of these substances in human blood plasma.

REFERENCES

Ammann, A. A. 2007. Inductively coupled plasma mass spectrometry (ICP MS): a versatile tool. *Journal of Mass Spectrometry*, 42 (4): 419-427.

Athinarayanan, J., Alshatwi, A. A., Periasamy, V. S. and Al-Warthan, A. A. 2015. Identification of Nanoscale Ingredients in Commercial Food Products and their Induction of Mitochondrially Mediated Cytotoxic Effects on Human Mesenchymal Stem Cells. *Journal of Food Science*, 80 (2): N459-N464.

Aureli, F., D'Amato, M., Raggi, A. and Cubadda, F. 2015. Quantitative characterization of silica nanoparticles by asymmetric flow field flow fractionation coupled with online multiangle light scattering and ICP-MS/MS detection. *Journal of Analytical Atomic Spectrometry*, 30 (6): 1266-1273.

Bantz, C., Koshkina, O., Lang, T., Galla, H.-J., Kirkpatrick, C. J., Stauber, R. H. and Maskos, M. 2014. The surface properties of nanoparticles determine the agglomeration state and the size of the particles under physiological conditions. *Beilstein Journal of Nanotechnology*, 5: 1774-1786.

Barahona, F., Geiss, O., Urbán, P., Ojea-Jimenez, I., Gilliland, D. and Barrero-Moreno, J. 2015. Simultaneous Determination of Size and Quantification of Silica Nanoparticles by Asymmetric Flow Field-Flow Fractionation Coupled to ICPMS Using Silica Nanoparticles Standards. *Analytical Chemistry*, 87 (5): 3039-3047.

Barahona, F., Ojea-Jimenez, I., Geiss, O., Gilliland, D. and Barrero-Moreno, J. 2016. Multimethod approach for the detection and characterisation of food-grade synthetic amorphous silica nanoparticles. *Journal of Chromatography A*, 1432: 92-100.

Baranowska-Wójcik, E., Szwajgier, D., Oleszczuk, P. and Winiarska-Mieczan, A. 2020. Effects of Titanium Dioxide Nanoparticles Exposure on Human Health—a Review. *Biological Trace Element Research*, 193 (1): 118-129.

Bartczak, D., Davies, J., Gollwitzer, C., Krumrey, M. and Goenaga-Infante, H. 2018. Changes in silica nanoparticles upon internalisation by cells: size, aggregation/agglomeration state, mass- and number-based concentrations. *Toxicology Research*, 7 (2): 172-181.

Bartczak, D., Vincent, P. and Goenaga-Infante, H. 2015. Determination of Size- and Number-Based Concentration of Silica Nanoparticles in a Complex Biological Matrix by Online Techniques. *Analytical Chemistry*, 87 (11): 5482-5485.

BIOVIA, D. S. 2016b. Material Studio modelling (computer software).

Bocca, B., Caimi, S., Senofonte, O., Alimonti, A. and Petrucci, F. 2018. ICP-MS based methods to characterize nanoparticles of TiO_2 and ZnO in sunscreens with focus on regulatory and safety issues. *Science of The Total Environment*, 630: 922-930.

Bolea-Fernandez, E., Leite, D., Rua-Ibarz, A., Balcaen, L., Aramendía, M., Resano, M. and Vanhaecke, F. 2017. Characterization of SiO_2 nanoparticles by single particle-inductively coupled plasma-tandem mass spectrometry (SP-ICP-MS/MS). *Journal of Analytical Atomic Spectrometry*, 32 (11): 2140-2152.

Box, G. E. P. and Behnken, D. W. 1960. Some New Three Level Designs for the Study of Quantitative Variables. *Technometrics*, 2 (4): 455-475.

Bunhu, T., Kindness, A. and Martincigh, B. S. 2011. Determination of titanium dioxide in commercial sunscreens by inductively coupled plasma-optical emission spectrometry. *South African Journal of Chemistry*, 64: 139-143.

Cölfen, H. and Antonietti, M. 2000. Field-Flow Fractionation Techniques for Polymer and Colloid Analysis. In: Schmidt, M. ed. *New Developments in Polymer Analytics I*. Berlin, Heidelberg: Springer Berlin Heidelberg, 67-187. Available: https://doi.org/10.1007/3-540-48764-6_2 (Accessed 23/4/2020).

Commision, E. 2011. Commision Recommendation of 18 October 2011 on the definition of nanomaterial (text with EEA relevance) (2011/696/EU). *Official Journal of the European Union*, (275): 38-40.

Contado, C. 2017. Field flow fractionation techniques to explore the "nano-world". *Analytical and Bioanalytical Chemistry*, 409 (10): 2501-2518.

Contado, C., Ravani, L. and Passarella, M. 2013. Size characterization by Sedimentation Field Flow Fractionation of silica particles used as food additives. *Analytica Chimica Acta*, 788: 183-192.

Dan, Y., Shi, H., Stephan, C. and Liang, X. 2015. Rapid analysis of titanium dioxide nanoparticles in sunscreens using single particle inductively coupled plasma–mass spectrometry. *Microchemical Journal*, 122: 119-126.

de la Calle, I., Menta, M., Klein, M., Maxit, B. and Séby, F. 2018. Towards routine analysis of TiO_2 (nano-)particle size in consumer products: Evaluation of potential techniques. *Spectrochimica Acta Part B: Atomic Spectroscopy*, 147: 28-42.

Dekkers, S., Krystek, P., Peters, R. J. B., Lankveld, D. P. K., Bokkers, B. G. H., van Hoeven-Arentzen, P. H., Bouwmeester, H. and Oomen, A. G. 2011. Presence and risks of nanosilica in food products. *Nanotoxicology*, 5 (3): 393-405.

Dubascoux, S., Von Der Kammer, F., Le Hécho, I., Gautier, M. P. and Lespes, G. 2008. Optimisation of asymmetrical flow field flow fractionation for environmental nanoparticles separation. *Journal of Chromatography A*, 1206 (2): 160-165.

Dudefoi, W., Villares, A., Peyron, S., Moreau, C., Ropers, M.-H., Gontard, N. and Cathala, B. 2018. Nanoscience and nanotechnologies for biobased materials, packaging and food applications: New opportunities and concerns. *Innovative Food Science & Emerging Technologies*, 46: 107-121.

Ferreira, S. L. C., Bruns, R. E., Ferreira, H. S., Matos, G. D., David, J. M., Brandão, G. C., da Silva, E. G. P., Portugal, L. A., dos Reis, P. S., Souza, A. S. and dos Santos, W. N. L. 2007. Box-Behnken design: An alternative for the optimization of analytical methods. *Analytica Chimica Acta*, 597 (2): 179-186.

Fiordaliso, F., Foray, C., Salio, M., Salmona, M. and Diomede, L. 2018. Realistic Evaluation of Titanium Dioxide Nanoparticle Exposure in Chewing Gum. *Journal of Agricultural and Food Chemistry*, 66 (26): 6860-6868.

Giddings, J. C. 1966. A New Separation Concept Based on a Coupling of Concentration and Flow Nonuniformities. *Separation Science*, 1 (1): 123-125.

Giese, B., Klaessig, F., Park, B., Kaegi, R., Steinfeldt, M., Wigger, H., von Gleich, A. and Gottschalk, F. 2018. Risks, Release and Concentrations of Engineered Nanomaterial in the Environment. *Scientific Reports*, 8 (1): 1565.

Goenaga-Infante, H. and Bartczak, D. 2020. Chapter 3.1.1 - Single particle inductively coupled plasma mass spectrometry (spICP-MS). In: Hodoroaba, V.-D., Unger, W. E. S. and Shard, A. G. eds. *Characterization of Nanoparticles*. Elsevier, 65-77. Available: http://www.sciencedirect.com/science/article/pii/B9780128141823000031 (Accessed 02/09/2020).

Gogos, A., Kaegi, R., Zenobi, R. and Bucheli, T. D. 2014. Capabilities of asymmetric flow field-flow fractionation coupled to multi-angle light scattering to detect carbon nanotubes in soot and soil. *Environmental Science: Nano*, 1 (6): 584-594.

Guilminot, E., Dalard, F. and Degrigny, C. 2002. Mechanism of iron corrosion in water–polyethylene glycol (PEG 400) mixtures. *Corrosion Science*, 44 (10): 2199-2208.

Hagendorfer, H., Kaegi, R., Parlinska, M., Sinnet, B., Ludwig, C. and Ulrich, A. 2012. Characterization of Silver Nanoparticle Products Using Asymmetric Flow Field Flow Fractionation with a Multidetector Approach – a Comparison to Transmission Electron Microscopy and Batch Dynamic Light Scattering. *Analytical Chemistry*, 84 (6): 2678-2685.

Han, S., Kim, C. and Kwon, D. 1997. Thermal/oxidative degradation and stabilization of polyethylene glycol. *Polymer*, 38 (2): 317-323.

Hanrahan, G. and Lu, K. 2006. Application of Factorial and Response Surface Methodology in Modern Experimental Design and Optimization. *Critical Reviews in Analytical Chemistry*, 36 (3-4): 141-151.

Hedayatnia, S., Mirhosseini, H., Tamnak, S. and Golpira, F. 2016. Improvement of Glass Transition and Flowability of Reduced-Fat Coffee Creamer: Effect of Fat Replacer and Fluidized Bed Drying. *Food and Bioprocess Technology*, 9 (4): 686-698.

Helsper, J. P. F. G., Peters, R. J. B., van Bemmel, M. E. M., Rivera, Z. E. H., Wagner, S., von der Kammer, F., Tromp, P. C., Hofmann, T. and Weigel, S. 2016. Physicochemical

characterization of titanium dioxide pigments using various techniques for size determination and asymmetric flow field flow fractionation hyphenated with inductively coupled plasma mass spectrometry. *Analytical and Bioanalytical Chemistry*, 408 (24): 6679-6691.

Heroult, J., Nischwitz, V., Bartczak, D. and Goenaga-Infante, H. 2014. The potential of asymmetric flow field-flow fractionation hyphenated to multiple detectors for the quantification and size estimation of silica nanoparticles in a food matrix. *Analytical and Bioanalytical Chemistry*, 406 (16): 3919-3927.

Hirpara, K. and Jana, A. 2011. Synergy of dairy with non-dairy Ingredients or product: A review. *African Journal of Food Science*, 5: 817-832.

ISO/TR 13014:2012. 2012. *Nanotechnologies — Guidance on physico-chemical characterization of engineered nanoscale materials for toxicologic assessment*. Available: https://www.iso.org/standard/52334.html (Accessed 05/03/2020).

ISO/TS 19590:2017. 2017. *Nanotechnologies — Size distribution and concentration of inorganic nanoparticles in aqueous media via single particle inductively coupled plasma mass spectrometry*. Available: https://www.iso.org/standard/65419.html (Accessed 24/02/2020).

Kanchi, S., Sabela, M. I., Singh, P. and Bisetty, K. 2017. Multivariate optimization of differential pulse polarographic–catalytic hydrogen wave technique for the determination of nickel(II) in real samples. *Arabian Journal of Chemistry*, 10: S2260-S2272.

Kim, S. T., Kim, H. K., Han, S. H., Jung, E. C. and Lee, S. 2013. Determination of size distribution of colloidal TiO_2 nanoparticles using sedimentation field-flow fractionation combined with single particle mode of inductively coupled plasma-mass spectrometry. *Microchemical Journal*, 110: 636-642.

Labille, J., Feng, J., Botta, C., Borschneck, D., Sammut, M., Cabie, M., Auffan, M., Rose, J. and Bottero, J. Y. 2010. Aging of TiO_2 nanocomposites used in sunscreen. Dispersion and fate of the degradation products in aqueous environment. *Environmental Pollution*, 158 (12): 3482-3489.

León, A., Reuquen, P., Garín, C., Segura, R., Vargas, P., Zapata, P. and Orihuela, P. A. 2017. FTIR and Raman Characterization of TiO_2 Nanoparticles Coated with Polyethylene Glycol as Carrier for 2-Methoxyestradiol. *Applied Sciences*, 7 (1): 49.

Lephalala, M., Kanchi, S., Sabela, M. I. and Bisetty, K. 2020. Electrochemical Enzymatic Biosensing of Neotame Supported by Computational Methods. *Electroanalysis*, 32: 1-13.

Lewicka, Z. A., Yu, W. W., Oliva, B. L., Contreras, E. Q. and Colvin, V. L. 2013. Photochemical behavior of nanoscale TiO_2 and ZnO sunscreen ingredients. *Journal of Photochemistry and Photobiology A: Chemistry*, 263: 24-33.

Lim, J.-H., Bae, D. and Fong, A. 2018. Titanium Dioxide in Food Products: Quantitative Analysis Using ICP-MS and Raman Spectroscopy. *Journal of Agricultural and Food Chemistry*, 66 (51): 13533-13540.

Lohrke, J., Briel, A. and Mäder, K. 2008. Characterization of superparamagnetic iron oxide nanoparticles by asymmetrical flow-field-flow-fractionation. *Nanomedicine*, 3 (4): 437-452.

Loosli, F., Wang, J., Rothenberg, S., Bizimis, M., Winkler, C., Borovinskaya, O., Flamigni, L. and Baalousha, M. 2019. Sewage spills are a major source of titanium dioxide engineered (nano)-particle release into the environment. *Environmental Science: Nano*, 6 (3): 763-777.

López-Heras, I., Madrid, Y. and Cámara, C. 2014. Prospects and difficulties in TiO_2 nanoparticles analysis in cosmetic and food products using asymmetrical flow field-flow fractionation hyphenated to inductively coupled plasma mass spectrometry. *Talanta*, 124: 71-78.

Lu, P.-J., Huang, S.-C., Chen, Y.-P., Chiueh, L.-C. and Shih, D. Y.-C. 2015. Analysis of titanium dioxide and zinc oxide nanoparticles in cosmetics. *Journal of Food and Drug Analysis*, 23 (3): 587-594.

Malm, A. V. and Corbett, J. C. W. 2019. Improved Dynamic Light Scattering using an adaptive and statistically driven time resolved treatment of correlation data. *Scientific Reports*, 9 (1): 13519.

Mano, S. S., Kanehira, K., Sonezaki, S. and Taniguchi, A. 2012. Effect of polyethylene glycol modification of TiO_2 nanoparticles on cytotoxicity and gene expressions in human cell lines. *Int J Mol Sci*, 13 (3): 3703-3717.

Manorama, S. V., Madhusudan Reddy, K., Gopal Reddy, C. V., Narayanan, S., Rajesh Raja, P. and Chatterji, P. R. 2002. Photostabilization of dye on anatase titania nanoparticles by polymer capping. *Journal of Physics and Chemistry of Solids*, 63 (1): 135-143.

Messaud, F. A., Sanderson, R. D., Runyon, J. R., Otte, T., Pasch, H. and Williams, S. K. R. 2009. An overview on field-flow fractionation techniques and their applications in the separation and characterization of polymers. *Progress in Polymer Science*, 34 (4): 351-368.

Metropolis, N., Rosenbluth, A. W., Rosenbluth, M. N., Teller, A. H. and Teller, E. 1953. Equation of State Calculations by Fast Computing Machines. *The Journal of Chemical Physics*, 21 (6): 1087-1092.

Moeta, P. J., Wesley-Smith, J., Maity, A. and Thwala, M. 2019. Nano-enabled products in South Africa and the assessment of environmental exposure potential for engineered nanomaterials. *SN Applied Sciences*, 1 (6): 577.

Montaño, M. D., Olesik, J. W., Barber, A. G., Challis, K. and Ranville, J. F. 2016. Single Particle ICP-MS: Advances toward routine analysis of nanomaterials. *Analytical and Bioanalytical Chemistry*, 408 (19): 5053-5074.

Mukherjee, A. and Hackley, V. A. 2018. Separation and characterization of cellulose nanocrystals by multi-detector asymmetrical-flow field-flow fractionation. *Analyst*, 143 (3): 731-740.

Müller, D., Nogueira, M., Cattaneo, S., Meier, F., Drexel, R., Contado, C., Pagnoni, A., de Vries, T., Cohen, D., Portugal-Cohen, M. and deMello, A. 2018. Integration of Inverse Supercritical Fluid Extraction and Miniaturized Asymmetrical Flow Field-Flow Fractionation for the Rapid Analysis of Nanoparticles in Sunscreens. *Analytical Chemistry*, 90 (5): 3189-3195.

Nischwitz, V. and Goenaga-Infante, H. 2012. Improved sample preparation and quality control for the characterisation of titanium dioxide nanoparticles in sunscreens using flow field flow fractionation on-line with inductively coupled plasma mass spectrometry. *Journal of Analytical Atomic Spectrometry*, 27 (7): 1084-1092.

Olesik, J. W. 1991. Elemental Analysis Using ICP-OES and ICP/MS. *Analytical Chemistry*, 63 (1): 12A-21A.

Oskam, G., Nellore, A., Penn, R. L. and Searson, P. C. 2003. The Growth Kinetics of TiO_2 Nanoparticles from Titanium(IV) Alkoxide at High Water/Titanium Ratio. *The Journal of Physical Chemistry B*, 107 (8): 1734-1738.

Pace, H. E., Rogers, N. J., Jarolimek, C., Coleman, V. A., Higgins, C. P. and Ranville, J. F. 2011. Determining Transport Efficiency for the Purpose of Counting and Sizing Nanoparticles via Single Particle Inductively Coupled Plasma Mass Spectrometry. *Analytical Chemistry*, 83 (24): 9361-9369.

Patterson, J. P., Sanchez, A. M., Petzetakis, N., Smart, T. P., Epps, I. I. I. T. H., Portman, I., Wilson, N. R. and O'Reilly, R. K. 2012. A simple approach to characterizing block copolymer assemblies: graphene oxide supports for high contrast multi-technique imaging. *Soft Matter*, 8 (12): 3322-3328.

Petersen, E. J. 2014. 9 - Ecotoxicological effects of carbon nanotubes: test methods and current research. In: Njuguna, J., Pielichowski, K. and Zhu, H. eds. *Health and Environmental Safety of Nanomaterials*. Woodhead Publishing, 175-199. Available: http://www.sciencedirect.com/science/article/pii/B978085709655550009X (Accessed 31/3/2020).

Postnova. 2016. *AF2000 MF: Operation Manual* Landsberg, Germany: Postnova Analytics GmbH.

Postnova. 2017. *NovaFFF AF2000: Software Manual* Landsberg, Germany: Postnova Analytics GmbH.

Rahim, S., Sasani Ghamsari, M. and Radiman, S. 2012. Surface modification of titanium oxide nanocrystals with PEG. *Scientia Iranica*, 19 (3): 948-953.

Selli, D., Tawfilas, M., Mauri, M., Simonutti, R. and Di Valentin, C. 2019. Optimizing PEGylation of TiO_2 Nanocrystals through a Combined Experimental and Computational Study. *Chemistry of Materials*, 31 (18): 7531-7546.

Shi, H., Magaye, R., Castranova, V. and Zhao, J. 2013. Titanium dioxide nanoparticles: a review of current toxicological data. *Particle and Fibre Toxicology*, 10 (1): 15.

Skočaj, M., Filipic, M., Petkovic, J. and Novak, S. 2011. Titanium dioxide in our everyday life; Is it safe? *Radiology and oncology*, 45: 227-247.

Stetefeld, J., McKenna, S. A. and Patel, T. R. 2016. Dynamic light scattering: a practical guide and applications in biomedical sciences. *Biophysical Reviews*, 8 (4): 409-427.

Sun, H. 1998a. COMPASS: an ab initio force-field optimized for condensed-phase applications overview with details on alkane and benzene compounds. *The Journal of Physical Chemistry B*, 102 (38): 7338-7364.

Sun, H. 1998b. COMPASS: An ab Initio Force-Field Optimized for Condensed-Phase ApplicationsOverview with Details on Alkane and Benzene Compounds. *The Journal of Physical Chemistry B*, 102 (38): 7338-7364.

Sun, H., Ren, P. and Fried, J. R. 1998. The COMPASS force field: parameterization and validation for phosphazenes. *Computational and Theoretical Polymer Science*, 8 (1): 229-246.

Takeuchi, T., Siswoyo, Aspanut, Z. and Wah Lim, L. 2009. Hydrodynamic Chromatography of Silica Colloids on Small Spherical Nonporous Silica Particles. *Analytical Sciences*, 25 (2): 301-306.

Tauler, R., Kowalski, B. and Fleming, S. 1993. Multivariate curve resolution applied to spectral data from multiple runs of an industrial process. *Analytical Chemistry*, 65 (15): 2040-2047.

Tayeb, A. M., Tony, M. A. and Mansour, S. A. 2018. Application of Box–Behnken factorial design for parameters optimization of basic dye removal using nano-hematite photo-Fenton tool. *Applied Water Science*, 8 (5): 138.

Tetteh, E. K., Naidoo, D. B. and Rathilal, S. 2019. Optimization of photo-catalytic degradation of oil refinery wastewater using Box-Behnken design. *Environmental Engineering Research*, 24 (4): 711-717.

Tucci, P., Porta, G., Agostini, M., Dinsdale, D., Iavicoli, I., Cain, K., Finazzi-Agró, A., Melino, G. and Willis, A. 2013. Metabolic effects of TiO_2 nanoparticles, a common component of sunscreens and cosmetics, on human keratinocytes. *Cell Death & Disease*, 4: e549.

Ulicny, J. and Kozar, T. 2018. Roadmap for Computer-Aided Modeling of Theranostics and Related Nanosystems. In: Proceedings of *EPJ Web of Conferences*. EDP Sciences, 05017.

Velimirovic, M., Wagner, S., Koeber, R., Hofmann, T. and von der Kammer, F. 2020a. Intra-laboratory assessment of a method for the detection of TiO_2 nanoparticles present in sunscreens based on multi-detector asymmetrical flow field-flow fractionation. *NanoImpact*, 19: 100233.

Velimirovic, M., Wagner, S., Monikh, F. A., Uusimäki, T., Kaegi, R., Hofmann, T. and Kammer, F. v. d. 2020b. Accurate quantification of TiO_2 nanoparticles in commercial

sunscreens using standard materials and orthogonal particle sizing methods for verification. *Talanta*, 215: 120921.

Verma, J. and Bhattacharya, A. 2018. Analysis on Synthesis of Silica Nanoparticles and its Effect on Growth of T. Harzianum & Rhizoctonia Species. *Biomedical Journal of Scientific & Technical Research*, 10: 7890-7897.

Voorhees, K. J., Baugh, S. F. and Stevenson, D. N. 1994. An investigation of the thermal degradation of poly(ethylene glycol). *Journal of Analytical and Applied Pyrolysis*, 30 (1): 47-57.

Wahlund, K. G. and Giddings, J. C. 1987. Properties of an asymmetrical flow field-flow fractionation channel having one permeable wall. *Analytical Chemistry*, 59 (9): 1332-1339.

Walters, C., Keeney, A., Wigal, C. T., Johnston, C. R. and Cornelius, R. D. 1997. The Spectrophotometric Analysis and Modeling of Sunscreens. *Journal of Chemical Education*, 74 (1): 99.

Willden, C. and Jensen, W. A. 2020. Optimal designs with axial values. *Journal of Quality Technology*, 52 (3): 235-248.

Wilschefski, S. C. and Baxter, M. R. 2019. Inductively Coupled Plasma Mass Spectrometry: Introduction to Analytical Aspects. *The Clinical Biochemist Reviews*, 40 (3): 115-133.

Winkler, H. C., Kornprobst, J., Wick, P., von Moos, L. M., Trantakis, I., Schraner, E. M., Bathke, B., Hochrein, H., Suter, M. and Naegeli, H. 2017. MyD88-dependent pro-interleukin-1β induction in dendritic cells exposed to food-grade synthetic amorphous silica. *Particle and Fibre Toxicology*, 14 (1): 21.

Winkler, H. C., Suter, M. and Naegeli, H. 2016. Critical review of the safety assessment of nano-structured silica additives in food. *Journal of Nanobiotechnology*, 14 (1): 44.

Wu, L., Yick, K.-l., Ng, S.-p. and Yip, J. 2012. Application of the Box–Behnken design to the optimization of process parameters in foam cup molding. *Expert Systems with Applications*, 39 (9): 8059-8065.

Wyatt, P. J. 2014. Measurement of Special Nanoparticle Structures by Light Scattering. *Analytical Chemistry*, 86 (15): 7171-7183.

Wyatt, P. J. 2018. Measuring nanoparticles in the size range to 2000 nm. *Journal of Nanoparticle Research*, 20 (12): 322.

Zaban, A., Aruna, S. T., Tirosh, S., Gregg, B. A. and Mastai, Y. 2000. The Effect of the Preparation Condition of TiO_2 Colloids on Their Surface Structures. *The Journal of Physical Chemistry B*, 104 (17): 4130-4133.

Zhang, H. and F. Banfield, J. 1998. Thermodynamic analysis of phase stability of nanocrystalline titania. *Journal of Materials Chemistry*, 8 (9): 2073-2076.

Zhang, M., Lei, J., Shi, Y., Zhang, L., Ye, Y., Li, D. and Mu, C. 2016. Molecular weight effects of PEG on the crystal structure and photocatalytic activities of PEG-capped TiO_2 nanoparticles. *RSC Advances*, 6 (86): 83366-83372.

Zhao, B., Yang, T., Zhang, Z., Hickey, M. E. and He, L. 2018a. A Triple Functional Approach To Simultaneously Determine the Type, Concentration, and Size of Titanium Dioxide Particles. *Environmental Science & Technology*, 52 (5): 2863-2869.

Zhao, L., Zhu, Y., Chen, Z., Xu, H., Zhou, J., Tang, S., Xu, Z., Kong, F., Li, X., Zhang, Y., Li, X., Zhang, J. and Jia, G. 2018b. Cardiopulmonary effects induced by occupational exposure to titanium dioxide nanoparticles. *Nanotoxicology*, 12 (2): 169-184.

Zhao, Q., Luan, X., Zheng, M., Tian, X.-H., Zhao, J., Zhang, W.-D. and Ma, B.-L. 2020. Synergistic Mechanisms of Constituents in Herbal Extracts during Intestinal Absorption: Focus on Natural Occurring Nanoparticles. *Pharmaceutics*, 12 (2): 128.

Zhou, D., Ji, Z., Jiang, X., Dunphy, D. R., Brinker, J. and Keller, A. A. 2013. Influence of material properties on TiO_2 nanoparticle agglomeration. *PloS one*, 8 (11): e81239-e81239.

Zhu, S., Ji, T., Yang, B. and Yang, Z. 2019. Preparation and characterization of PEG/surface-modified layered double hydroxides as a new shape-stabilized phase change material. *RSC Advances*, 9 (41): 23435-23443.

Zimm, B. H. 1948. Apparatus and Methods for Measurement and Interpretation of the Angular Variation of Light Scattering; Preliminary Results on Polystyrene Solutions. *The Journal of Chemical Physics*, 16 (12): 1099-1116.

Zulfah, N. L. and Siripinyanond, A. 2018. Investigation of tin adsorption on silica nanoparticles by using flow field-flow fractionation with offline inductively coupled plasma mass spectrometry. *Journal of Analytical Science and Technology*, 9 (1): 19.

APPENDICES

Appendix 1. Lists of ingredients for respective commercial SPF 50 sunscreens.

"Nano" SPF 50 Sunscreen	**"Unspecified" SPF 50 Sunscreen**
Aqua, Homosalate, Octocrylene, Glycerin, Butyl Methoxydibenzoylmethane, Ethylhexyl Salicylate, Alcohol Denat., Bis-Ethylhexyloxyphenol Methoxyphenyl Triazine, **Titanium Dioxide (Nano)**, Cetearyl Alcohol, Glyceryl Stearate SE, Myristyl Myristate, Sodium Phenylbenzimidazole Sulfonate, Glyceryl Glucoside, Tocopheryl Acetate, VP/Hexadecene Copolymer, C18-38 Alkyl Hydroxystearoyl Stearate, Sodium Cetearyl Sulfate, Xanthan Gum, Sodium Acrylates/C10-30 Alkyl Acrylate Crosspolymer, Silica Dimethyl Silylate, Trimethoxycaprylylsilane, Trisodium EDTA, Phenoxyethanol, Methylparaben, Linalool, Limonene, Butylphenyl Methylpropional, Benzyl Alcohol, Alpha-Isomethyl Ionone, Citronellol, Eugenol, Coumarin, Parfum	Water, Octocrylene Homosolate, Butyl Methoxydibenzoylmethane, Ethylhexyl Salicylate, Benzophenone-3, Potassium Cetyl Phosphate, PVP/Eicosene Copolymer, Alcohol Denat, Bis-Ethylhexyloxyphenol Methoxyphenyl Triazine, Polymethyl Acrylate, C12-15 Alkyl Benzoate, Cetearyl Alcohol, PEG-8, Myristyl Myristate, Octyldodecanol, **Titanium Dioxide**, Vitis Vinifera (Grape) Seed Extract, Vaccinum Oxycoccos (Cranberry) Extract, Lycium Chinese Fruit Extract, Tocopheryl Acetate, Glycerin, Propylene Glycol, PEG-40 Hydrogenated Castor Oil, Glycereth-26, Xanthan Gum, Acrylates/C10-30 Alkyl Acrylate Crosspolymer, Neopentyl Glycol Dicaprylate/Dicaprate, Isopropyl Palmitate, Sodium Laureth Sulfate, Amino Methyl Propanol, Triethanolamine, Glyceryl Stearate, PEG-40 Stearate, Ceteareth-20, Aluminum Stearate, Polyhydroxystearic Acid, Alumina, Disodium EDTA, BHT, Citric Acid, Sodium Benzoate, Sodium Sorbate, Fragrance, Methylisothiazolinone, Decylene Glycol, Caprylyl Glycol,

	Phenoxyethanol, Benzyl Salicylate, Citronellol, Geraniol, Hydroxyisohexyl 3-Cyclohexene, Carboxaldehyde, Linalool.

Appendix 2. Lists of ingredients for respective commercial coffee creamers.

Sample A	**Sample B**	**Sample C**
Glucose Syrup, Hydrogenated Vegetable Oil (Palm Kernel and Palm Fruit) and/or Non-hydrogenated Vegetable Oil (Palm Kernel and Palm Fruit), Casein [(Milk Protein) Lactose Free], Di-potassium Phosphate (E340), Hydrolysed Wheat Protein (Gluten), Distilled Monoglycerides (E471), **Free Flow Agent (E551)**.	Glucose, Hydrogenated vegetable fat [palm fruit, antioxidant: BHA (E320)], Lactic casein (cow's milk), Emulsifier (E471), **Anticaking agent (E551)**, Stabiliser (E452), Acidity regulator (E524), Preservative: Potassium metabisulphite (E224).	Glucose Syrup Solids, Vegetable Oil (Palm Kernel, Palm Fruit), Stabilisers (E340, E331, E452), Hydrolysed Wheat Protein (Gluten), Sodium Caseinate (a milk derivative), Emulsifier (E481), Salt, **Anticaking Agent (E551)**, Flavouring, Colourants (E101i, E160a).

Appendix 3. Pre-experimental variable values for SiO_2 NP multivariate analysis.

Crossflow (ml/min)	**Injection Time (min)**	**Sonication Time (min)**
0.8	3	10
1	3.5	16.25
1.2	4	22.5
1.4	4.5	28.75
1.6	5	35
1.8	5.5	41.25
2	6	47.5
2.2	6.5	53.75
2.4	7	60